# Impact of control noise on a variational quantum eigensolver

by

Xinning Wang

A thesis
presented to the University of Waterloo
in fulfillment of the
thesis requirement for the degree of
Master of Science
in
Chemistry (Quantum Information)

Waterloo, Ontario, Canada, 2025

© Xinning Wang 2025

## Author's Declaration

This thesis consists of material all of which I authored or co-authored: see Statement of Contributions included in the thesis. This is a true copy of the thesis, including any required final revisions, as accepted by my examiners.

I understand that my thesis may be made electronically available to the public.

## Statement of Contributions

This thesis contains work carried out in collaboration with members of our research group. The quantum-dot simulator used throughout this thesis is a large collaborative software project developed within the group. A non-exhaustive list of contributors to the simulator at different stages includes Bohdan Khromets, Brandon Buonacorsi, Stephen Harrigan, Zach Merino, and Xinning Wang.

My own contributions to the simulator include developing modules for simulating various noise models (e.g., random telegraph noise and $1/f$ noise), implementing voltage-miscalibration modeling, and creating functions for quantum process tomography and fidelity calculations. I also performed extensive beta testing of `QuDiPy`, providing bug reports and validation of new features against analytical predictions. All simulations presented in this thesis were executed by me using the simulator.

Chapter 2 presents the method for calculating unitary errors. This builds upon the foundational approach developed by Bohdan Khromets, to which I contributed by implementing the procedure in code, extending it to support multiple noise types, and integrating it with the tomography framework.

In Chapter 3, the section *Impact of Voltage Miscalibration on Gate Fidelity* includes a theoretical derivation of the RX gate fidelity under miscalibration, carried out in close collaboration with Bohdan Khromets. He provided the initial conceptual framework, while I performed the full symbolic derivations, validated them numerically, and prepared the final figures.

The section *VQE Simulation – Hydrogen Molecule* in Chapter 3 describes the application of the variational quantum eigensolver. Bohdan Khromets led the simplification of the VQE circuit diagram.

## Abstract

Quantum computers promise advantages over classical systems for problems such as molecular simulation, fueling the development of hybrid quantum-classical algorithms like the Variational Quantum Eigensolver (VQE). VQE is particularly attractive for noisy intermediate-scale quantum (NISQ) devices due to its shallow circuit depth and partial resilience to noise. Silicon-based spin qubits, with their compatibility with existing semiconductor technologies, are strong candidates for scalable quantum computation. However, their performance is constrained by hardware imperfections—chiefly charge noise and voltage miscalibration—that manifest as fluctuations or offsets in gate electrode voltages. These disturbances degrade quantum gate fidelities and, in turn, the accuracy of algorithmic results, presenting significant challenges for practical applications.

In this thesis, we develop a comprehensive hardware-algorithm co-simulation framework to quantify the impact of voltage noise on silicon quantum dot systems. Charge noise is modeled using an ensemble of random telegraph noise processes to emulate realistic $1/f$-like spectra. We systematically investigate the effects of stochastic noise and systematic miscalibration at both the gate level and algorithm level. For individual quantum gates—including $RX(\pi/2)$, Hadamard, CZ, and $\sqrt{\text{SWAP}}$—we characterize noise-induced fidelity loss and derive analytical expressions for error sensitivity, revealing contrasting robustness between detuning-driven and exchange-driven gates. Quantum process tomography and Kraus operator decomposition further elucidate dominant error channels, distinguishing coherent and incoherent contributions from different noise regimes.

Extending the analysis to algorithm performance, we simulate VQE for the hydrogen molecule and identify a practical noise tolerance window within which high-accuracy energy estimation is maintained.

These advances underscore the progress in bridging device physics and quantum algorithm implementation for silicon spin qubits, offering quantitative guidance on error budgeting, control calibration, and the development of noise-resilient algorithms for near-term quantum processors.

**Acknowledgements**

First and foremost, I would like to thank my supervisor, Prof. Jonathan Baugh, for his patient guidance, encouragement, and invaluable insights throughout my graduate studies. His support and mentorship have been instrumental in shaping my academic journey. I am deeply grateful to Bohdan Khromets for his generous help and advice during my research, and to Zach Merino for his support in the early stages, when he took the time to explain so many of the foundational concepts that helped me get started. I also wish to thank all the members of our group for creating such a friendly, welcoming, and collaborative environment. Their kindness and willingness to help have made my time in the lab truly enjoyable.

Finally, I am profoundly thankful to my family and friends for their unwavering support and encouragement. Their belief in me made this journey possible.

## Dedication

To my parents and siblings, for their unconditional love and support.

# Table of Contents

**Author's Declaration** ii

**Statement of Contributions** iii

**Abstract** iv

**Acknowledgements** v

**Dedication** vi

**List of Figures** x

**List of Tables** xiv

**List of Abbreviations** xv

**1 Introduction** 1

1.1 Quantum Computing . . . . . 1

1.2 Quantum Dots: Spin Qubits . . . . . 2

1.2.1 Single Quantum Dot: Electrostatic Confinement and Spin Qubit Formation . . . . . 2

1.2.2 Double Quantum Dot: Detuning, Tunnel Coupling, and Exchange Interaction . . . . . 3

1.2.3 Single-spin Control in Silicon MOS Quantum Dots . . . . . 6
1.2.4 Two-qubit Gates via Exchange Coupling . . . . . 7
1.3 Key Challenges . . . . . 8
1.3.1 Gate Miscalibration in Quantum Dot Systems . . . . . 8
1.3.2 The Challenge of Charge Noise in Spin Qubits . . . . . 9

**2 Methods** **11**
2.1 Spin Qubit Simulator . . . . . 11
2.2 Modeling Charge Noise via Random Telegraph Noise . . . . . 13
2.3 Quantum Process Tomography . . . . . 18
2.3.1 Error Process Matrix and Kraus Representation . . . . . 20
2.3.2 Unitary Error . . . . . 21

**3 Effects of noise on quantum gate operations** **24**
3.1 Impact of Voltage Miscalibration on Gate Fidelity . . . . . 24
3.2 Random Telegraph Noise Effect on a Single Gate . . . . . 33
3.3 Error Analysis via Quantum Process Tomography . . . . . 36

**4 Noise Analysis in Variational Quantum Eigensolvers** **45**
4.1 Variational Quantum Eigensolvers . . . . . 45
4.1.1 Variational Quantum Eigensolvers Simulation - Hydrogen Molecule 49
4.2 Impact of Noise on Ground-state Energy . . . . . 52
4.2.1 Impact of Miscalibration on Variational Quantum Eigensolvers . . . 52
4.2.2 Impact of Random Telegraph Noise on Variational Quantum Eigensolvers . . . . . 55

**5 Conclusions and future work** **58**
5.1 Conclusions . . . . . 58
5.2 Future Work . . . . . 59

**References** **61**

**APPENDICES** **68**

**A Coefficients for $R = 1.4$ Å** **69**

# List of Figures

1.1 (a) Top-down schematic of a silicon MOS double quantum dot device with plunger (P), tunnel (T), and lead (L) gates managing source (S) and drain (D) connections. (b) Reduced 3D model of a four-dot device for finite-element Poisson simulations, showing four plunger gates (P1–P4, $V_1$–$V_4$) and three tunnel gates (T1–T3, $W_1$–$W_3$) shaping the electrostatic potential in the 2DEG plane. . . . . 4

2.1 Characteristics of random telegraph noise. **(a)** Time-domain trace of a single RTN realization with amplitude $A = 1\,\mathrm{mV}$ and symmetric switching time $\langle\tau_0\rangle = \langle\tau_1\rangle = 100\,\mathrm{ns}$. **(b)** Power spectral density (PSD) from 20 summed and normalized RTN realizations with the same parameters as in (a). The black line shows the theoretical Lorentzian PSD with $1/f^2$ decay at high frequencies. The blue dashed line indicates the cutoff frequency $f_c$. . . . . 14

2.2 Power spectral densities (PSDs) of RTN traces generated with fixed amplitude $A = 1\,\mathrm{mV}$ and varying switching times $\tau$. Each curve shows the PSD from 50 summed and normalized RTN realizations for $\tau = \tau_0 = \tau_1 \in \{10^{-8}, 10^{-7}, 10^{-6}, 10^{-5}, 10^{-4}\}\,\mathrm{s}$. Increasing $\tau$ shifts the cutoff frequency $f_c = (2\pi\tau)^{-1}$ to lower values, illustrating the transition from fast to quasistatic noise. . . . . 16

2.3 Comparison of SWAP gate voltage waveforms with and without simulated charge noise. The noise is generated by summing 50 independent RTN traces per electrode and normalizing to preserve the spectral profile, then added directly to the ideal control pulses. The pulse uses a wide Gaussian envelope with a total duration of $10\,\mu\mathrm{s}$. (a) Ideal gate voltage. (b) Gate voltages with a superimposed noise sequence ($A = 2\,\mathrm{mV}$, $\tau = 100\,\mathrm{ns}$). . . . . 17

2.4 Schematic of SQPT. A complete set of linearly independent input states $\rho_i$ is prepared and passed through the unknown quantum process $\mathcal{E}$. The resulting output states are measured using quantum state tomography, enabling reconstruction of the process matrix $\chi$. . . . . 19

2.5 Error process matrices $\chi^{\text{err}}$ for the $RX(\pi/2)$ gate on qubit 1. Color bars indicate matrix element amplitudes in the Pauli basis. (a) Ideal case ($\chi^{\text{err}}_{00} = 1$) showing no noise. (b) RTN noise with amplitude $3.5 \times 10^{-3}\,\text{V}$ and $\tau = 1\,\mu\text{s}$, averaged over 100 realizations. For clarity, $\chi^{\text{err}}_{00}$ is set to zero. . . . . 22

3.1 Simulated gate infidelity under voltage miscalibration. Each data point represents the average of 800 samples with Gaussian-distributed multiplicative ($a$) and additive ($b$) voltage noise. Error bars indicate the $20^{\text{th}}$–$80^{\text{th}}$ percentile range of the cumulative distribution of simulated fidelities, providing a measure of variability across noise realizations. **(a)** RX($\pi/2$) gate; **(b)** Hadamard gate; **(c)** CZ gate; **(d)** $\sqrt{\text{SWAP}}$ gate. . . . . 27

3.2 Analytically calculated fidelities of RX and $\sqrt{\text{SWAP}}$ gates as a function of $\sigma_b$ for several fixed $\sigma_a$ values. . . . . 32

3.3 Log-log plots of gate infidelity under RTN. Each curve corresponds to a fixed RTN switching time $\tau$ from $10^{-8}\,\text{s}$ to $10^{-4}\,\text{s}$. The vertical axis shows $\log_{10}(1 - F)$, and the horizontal axis shows RTN amplitude in millivolts. . 34

3.4 Kraus operator norms versus noise amplitude for three representative gates: CZ, RX($\pi/2$), and Hadamard. Each panel shows the six dominant Kraus operators ($K_1$–$K_6$), where $K_6$ corresponds to the operator with the largest norm. For $K_6$, we plot $1 - \|K_6\|$. The norms are computed after undoing the respective ideal unitary from each Kraus operator. . . . . 39

3.5 Pauli decomposition of the six Kraus operators for the CZ gate under voltage noise. The top panel shows dominant Pauli coefficients for each Kraus operator as a function of noise amplitude, displaying only terms exceeding a threshold of 0.005 at maximum amplitude. The bottom table summarizes linear fits for the first five Kraus operators. The first column lists the Norm scale (effective strength) of each Kraus operator, and the second column shows the normalized dominant Pauli error terms. Coefficients are computed after undoing the gate unitary transformation (applying $U^{\dagger}_{\text{gate}}$). 40

3.6 Pauli decomposition of the six Kraus operators for the RX gate under voltage noise. The top panel shows dominant Pauli coefficients for each Kraus operator as a function of noise amplitude, displaying only terms exceeding a threshold of 0.001 at maximum amplitude. The bottom table summarizes linear fits for the first five Kraus operators. The first column lists the Norm scale (effective strength) of each Kraus operator (the product of the common fit factor and a normalization factor), and the second column shows the normalized dominant Pauli error terms. Coefficients are computed after undoing the gate unitary transformation (applying $U_{\text{gate}}^{\dagger}$). . . . . 41

3.7 Pauli decomposition of the six dominant Kraus operators for the Hadamard gate under voltage noise. The top panel shows the dominant Pauli coefficients (threshold = 0.001) as a function of noise amplitude, for the six Kraus operators with the largest norms. The bottom table summarizes linear fits for the first five Kraus operators. The first column lists the Norm scale (effective strength) of each Kraus operator, and the second column shows the normalized dominant Pauli error terms. Coefficients are computed after undoing the Hadamard unitary transformation. . . . . 42

3.8 CZ gate fidelity vs. RTN amplitude. (a): $\tau = 10^{-7}$ s. (b): $\tau = 10^{-8}$ s. Blue: before correction; orange: after correction. . . . . 43

4.1 VQE Pipeline (1) Preparation steps: (a) Express the given Hamiltonian as a quantum observable wavefunction; (b) Encode from fermionic space to Pauli space; (2) Find initial state: Usually use Hartree-Fock method; (3) Ansatz Selection: Prepare trial state with selected ansatz; (4) Measurements; (5) Parameter Update: Optimize the parameter on the classical computer. . . 46

4.2 Hydrogen molecule with nuclei separated by distance R . . . . . 49

4.3 VQE circuit of the chemically-inspired UCC ansatz . . . . . 51

4.4 VQE simulation results: (a) Energy landscape of the variational optimization process for selected internuclear distances. (b) Ground-state energy curve from VQE simulations, compared with FCI reference values. . . . . 52

4.5 Effect of voltage miscalibration on VQE energy estimation from 600 independent VQE trials. (a) Average estimated energy $\langle E \rangle$ as a function of miscalibration strengths $\sigma_a$ and $\sigma_b$. (b) Standard deviation $\sigma_E$ of the energy estimates, showing increased fluctuations under noise. (c) Cross-sections of bar plots for $\langle E \rangle$ from (a) and (b), showing the dependence on $\sigma_b$ (with $\sigma_a$ fixed) and $\sigma_a$ (with $\sigma_b$ fixed). (d) Distribution of energy estimates for $\sigma_a = 0.002$, $\sigma_b = 0.0002$, fitted with a gamma distribution. The Kolmogorov–Smirnov (KS) test yields $p = 0.855$; since $p > 0.05$, there is no statistically significant deviation from the gamma fit, indicating a good agreement. . . . . 54

4.6 Relative error in the ground-state energy of the hydrogen molecule as a function of the RTN correlation time $\tau$, for three noise amplitudes $A$. The error bars represent standard deviations over 40 independent VQE runs. . 56

# List of Tables

3.1 Quadratic fit coefficients $a$ for all gates at different $\tau$. . . . . 35
3.2 Relative infidelity improvement for the CZ gate at $A = 1\,\mathrm{mV}$. . . . . 43

A.1 Coefficients for $R = 1.4\,\text{Å}$ computed using Psi4. . . . . 69

# List of Abbreviations

**QPT** Quantum Process Tomography 18, 20, 21, 24, 36, 58

**RTN** Random Telegraph Noise 13–15, 21, 24, 33, 35, 55, 58

**VQE** Variational Quantum Eigensolver 45–47, 49, 52, 53, 55

# Chapter 1

# Introduction

## 1.1 Quantum Computing

Quantum computing holds great promise in tackling problems that are intractable for classical computers, particularly in domains such as quantum chemistry, materials science, and cryptography [1, 2, 3, 4, 5]. During the past decade, advances in both theory and hardware have led to the experimental demonstration of small-scale quantum algorithms and the quantum advantage [6, 7, 8]. A wide range of physical platforms—including superconducting circuits, trapped ions, photonic systems, and semiconductor-based devices—have been proposed and developed to realize scalable quantum processors [9, 10, 11, 12, 13].

Across all these platforms, one of the most critical challenges is achieving high-fidelity quantum gate operations. Physical qubits are inherently susceptible to environmental noise and control imperfections, which can lead to both coherent and incoherent errors [14, 15, 16]. Solid-state architectures, such as silicon-based quantum dots, are particularly sensitive to certain types of error sources, including charge noise and calibration drift, due to their reliance on precise electrostatic control.

Despite these challenges, silicon quantum dot qubits are considered a promising path toward scalable quantum computing, thanks to their compatibility with CMOS fabrication, potential for dense integration, and long coherence times [17, 18]. These advantages make it especially important to understand and mitigate noise mechanisms in this platform, where small voltage fluctuations can significantly impact gate performance. In this chapter, we begin by introducing the fundamental physical principles of quantum dot spin qubits, which serve as the foundation for our subsequent analysis of noise mechanisms and strategies for their mitigation.

## 1.2 Quantum Dots: Spin Qubits

Among the various physical qubit implementations, semiconductor quantum dot spin qubits stand out for their scalability, compatibility with CMOS fabrication, and ability to operate at relatively high temperatures [17]. In these systems, electrons are confined within electrostatically defined potential wells, known as quantum dots, created by applying voltages to patterned metal gates on a two-dimensional electron gas (2DEG), typically formed at the $Si/SiO_2$ interface in metal-oxide-semiconductor (MOS) structures. When the confinement length scale becomes comparable to the electron's Fermi wavelength, the energy levels within the dot become quantized, allowing the system to behave as an artificial atom [19].

The spin degree of freedom of a single confined electron forms a quantum bit, enabling quantum information to be encoded, manipulated, and measured. These qubits can be controlled using magnetic fields, electric fields, or a combination of both, depending on the device design. Additional flexibility and tunability can be introduced using double or triple quantum dot structures, which enable exchange-based operations and multi-spin encoding schemes.

Despite a diversity of device architectures, the underlying theoretical principles remain consistent: gate-induced confinement in layered semiconductor interfaces leads to quantized energy levels suitable for defining two-level quantum systems. The remainder of this section builds on these principles to examine how a controllable two-level spin qubit system can be isolated and operated within such a framework.

### 1.2.1 Single Quantum Dot: Electrostatic Confinement and Spin Qubit Formation

In silicon metal-oxide-semiconductor (Si-MOS) architectures, the silicon substrate is undoped, so no two-dimensional electron gas (2DEG) exists at the $Si/SiO_2$ interface under equilibrium conditions. When a positive bias is applied to lithographically defined surface gates, electrons are locally accumulated at the interface, inducing a 2DEG. By further adjusting the voltages on specific gate electrodes, regions of the 2DEG can be shaped into isolated potential wells that trap individual electrons, effectively defining quantum dots. The gate layout typically includes plunger (P) gates to control electron occupancy, tunnel (T) gates to tune interdot coupling, and lead (L) gates to manage connections to external reservoirs (source and drain), as illustrated in Fig. 1.1(a).

To better visualize the electrostatic environment in these devices, Fig. 1.1(b) shows a reduced three-dimensional model geometry used for finite-element Poisson calculations of the potential landscape. In this model, four plunger gates (P1–P4) with applied voltages $V_1$–$V_4$ and three tunnel gates (T1–T3) with voltages $W_1$–$W_3$ define the confinement and tunnel barriers. The resulting 3D potential profile illustrates how gate-induced fields shape the confinement wells in the plane of the induced 2DEG.

Once confined, the dot's charge occupation is governed by Coulomb blockade physics. The addition of a single electron costs an electrostatic charging energy $E_C = e^2/C$, where $C$ is the total capacitance of the dot. The electrochemical potential for adding the $N$th electron is [20]:

$$\mu(N, V_g) = E_C \left( N - N_0 - \frac{1}{2} - \frac{C_g V_g}{e} \right),$$

where $V_g$ is the applied gate voltage, $C_g$ the gate-dot capacitance, and $N_0$ the reference electron number at zero bias. When the tunnel resistance between the dot and its leads exceeds $h/e^2$, the electron number becomes fixed, enabling stable charge configurations.

In addition to Coulomb blockade, lateral confinement quantizes the orbital energy levels within the dot. The level spacing scales as $\Delta E \sim \hbar^2/(2m^*R^2)$, where $m^*$ is the effective mass of the electron in silicon and $R$ is the dot radius. At cryogenic temperatures (typically below 100 mK), thermal excitation is suppressed, and electrons occupy only the lowest orbital levels, with each level accommodating up to two electrons of opposite spin due to the Pauli exclusion principle.

To encode a spin qubit, the system is tuned to the single-electron regime ($N = 1$). A static magnetic field is applied to lift spin degeneracy via the Zeeman effect, resulting in an energy splitting $\Delta E_Z = g\mu_B B$ between spin-up and spin-down states. These two spin states define a well-isolated, controllable two-level quantum system. The low nuclear spin density of silicon and its compatibility with CMOS processes make spin qubits in this material highly promising for scalable quantum computing platforms.

### 1.2.2 Double Quantum Dot: Detuning, Tunnel Coupling, and Exchange Interaction

Consider a double quantum dot (DQD) system hosting a single electron, with the charge configuration either $(1, 0)$ or $(0, 1)$, where $(1, 0)$ denotes one electron localized in the left dot and $(0, 1)$ in the right dot [21]. This charge degree of freedom forms the basis for coherent charge manipulation.

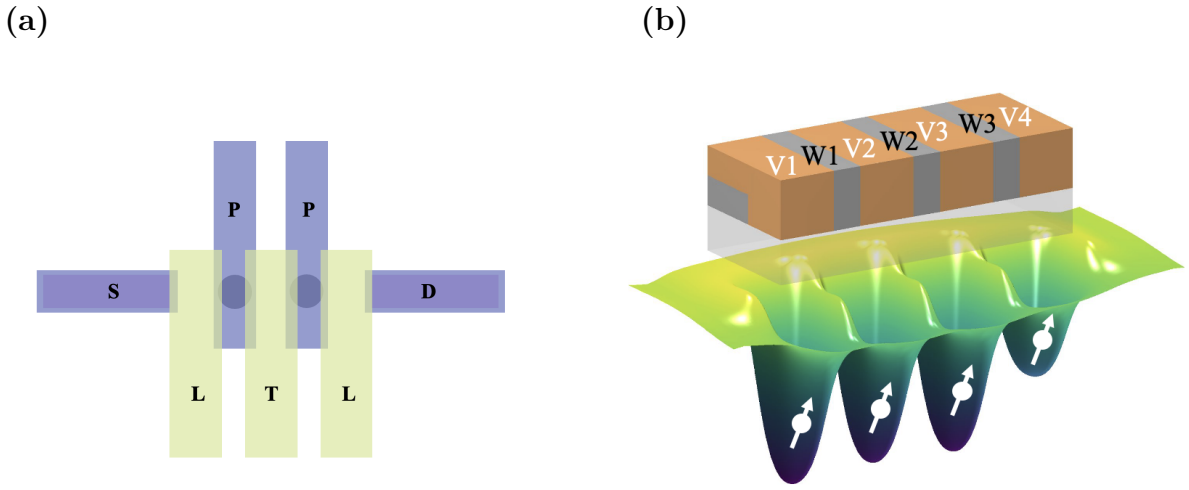



Figure 1.1: (a) Top-down schematic of a silicon MOS double quantum dot device with plunger (P), tunnel (T), and lead (L) gates managing source (S) and drain (D) connections. (b) Reduced 3D model of a four-dot device for finite-element Poisson simulations, showing four plunger gates (P1–P4, $V_1$–$V_4$) and three tunnel gates (T1–T3, $W_1$–$W_3$) shaping the electrostatic potential in the 2DEG plane.

In quantum computing applications, DQD systems are typically operated in the $(1,1)$ regime, where each dot contains one electron spin. The electrostatic potentials of the two dots are controlled by gate voltages $V_{g,L}$ and $V_{g,R}$ applied to plunger gates, with corresponding gate-dot capacitances $C_{g,L}$ and $C_{g,R}$, and total dot capacitances $C_L$ and $C_R$. Neglecting cross-capacitance, the energy difference between the two charge configurations is given by [22]:

$$\Delta E = U(0,1) - U(1,0) = e\left(\frac{V_{g,L}C_{g,L}}{C_L} - \frac{V_{g,R}C_{g,R}}{C_R}\right) + \text{const.} \tag{1.1}$$

This motivates the definition of the detuning parameter $\varepsilon$, the energy difference between dots induced by gate voltages:

$$\varepsilon = \alpha_R V_{g,R} - \alpha_L V_{g,L} + E_0, \tag{1.2}$$

where $\alpha_{L,R} = eC_{g,(L,R)}/C_{L,R}$ are lever arms converting gate voltages to energies, and $E_0$ is a constant offset. Detuning $\varepsilon$ is the key control parameter for tuning the charge energy landscape.

The interdot tunnel coupling describes the coherent hybridization between $|(1,0)\rangle$ and $|(0,1)\rangle$ states. Denoting this single-electron tunneling amplitude as $t_c$, the tunnel Hamiltonian reads:

$$H_T = t_c \left|(1,0)\right\rangle \left\langle(0,1)\right| + \text{h.c.} \tag{1.3}$$

In the $\{|(1,0)\rangle, |(0,1)\rangle\}$ basis, the total Hamiltonian is:

$$H = \begin{pmatrix} \varepsilon/2 & t_c \\ t_c & -\varepsilon/2 \end{pmatrix}. \tag{1.4}$$

Its eigenenergies

$$E_{g,e} = \mp\sqrt{\left(\frac{\varepsilon}{2}\right)^2 + t_c^2} \tag{1.5}$$

describe the ground and excited hybridized charge states. At zero detuning $\varepsilon = 0$, the splitting is $2t_c$, with eigenstates formed by symmetric and antisymmetric superpositions of $|(1,0)\rangle$ and $|(0,1)\rangle$.

When spin degrees of freedom are included, the low-energy physics in the $(1,1)$ regime is dominated by spin-dependent interactions between electrons localized in each dot. The most important of these is the exchange interaction $J$, which quantifies the energy splitting between singlet and triplet spin states:

$$J = E_T - E_S = V - \frac{U_H}{2} + \frac{1}{2}\sqrt{U_H^2 + 16t_H^2}. \tag{1.6}$$

Here, $E_T$ and $E_S$ are the energies of the triplet and singlet states, respectively. The parameters $t_H$ and $U_H$ correspond to the *extended hopping matrix element* and the *on-site Coulomb repulsion energy*, respectively, both of which are renormalized by long-range Coulomb interactions beyond the standard short-range Hubbard model. The term $V$ denotes the direct interdot Coulomb interaction. This extended Hubbard model framework captures the low-energy spin physics in a double quantum dot by effectively incorporating electron-electron interaction corrections into the tunneling and Coulomb parameters.

In the extended Hubbard limit, where the ratio $t_H/U_H \ll 1$, Eq. 1.6 simplifies to:

$$J = \frac{4t_H^2}{U_H} + V. \tag{1.7}$$

Here, the first term $\frac{4t_H^2}{U_H}$ has the form of the standard Hubbard approximation, but with $t_H$ and $U_H$ renormalized by long-range Coulomb interactions [23]. The second term $V$ is an additional contribution that accounts for the difference in Coulomb energy between singly occupied singlet and triplet states.

It is important to distinguish between the bare tunnel coupling $t_c$, introduced earlier as the single-electron tunneling amplitude governing charge hybridization, and the effective tunnel coupling $t_H$, which appears in the exchange interaction. While $t_c$ reflects the direct

control of the interdot barrier by gate voltages in the charge Hamiltonian, $t_H$ represents a renormalized hopping matrix element within the extended Hubbard framework, accounting for long-range Coulomb interactions and electron correlations [23]. This distinction is crucial for accurately describing both charge and spin dynamics and for understanding how electrical tuning of gate voltages enables precise control over qubit operations in silicon DQD devices.

### 1.2.3 Single-spin Control in Silicon MOS Quantum Dots

In silicon metal-oxide-semiconductor (Si-MOS) architectures, single-spin qubits are encoded in the spin states $|\uparrow\rangle$ and $|\downarrow\rangle$ of a single electron confined within a quantum dot. Coherent manipulation of such qubits is achieved using electron spin resonance (ESR) techniques, wherein a static magnetic field $B_z$ defines the spin quantization axis and lifts the degeneracy of the spin states via the Zeeman effect. An additional oscillating magnetic field, typically in the microwave frequency range (5–50 GHz), is applied perpendicular to $B_z$ to drive Rabi oscillations around the Bloch sphere [22].

The ESR paradigm offers a straightforward and scalable control scheme, as a single on-chip coplanar waveguide (CPW) can globally deliver microwave magnetic fields across an array of qubits [24]. To achieve selective addressing, Si-MOS devices can exploit small variations in the electron $g$-factor induced by spin-orbit coupling and interface effects. These variations produce qubit-specific resonance frequencies (Stark shifts), enabling frequency multiplexing and simultaneous control within the global field. This approach avoids the heating and spatial crosstalk associated with high-power CPWs, which were limitations in earlier GaAs and silicon ESR implementations.

Alternatively, electric-dipole spin resonance (EDSR) techniques can be employed to achieve single-spin control without the need for oscillating magnetic fields [25]. Here, local gate electrodes displace the electron in the presence of a magnetic field gradient—typically provided by a nearby micromagnet—effectively converting charge motion into an oscillating magnetic field via the slanting-field mechanism. The use of micromagnets additionally introduces site-specific $B_z$ offsets, further enabling frequency-selective addressing under a global field.

Initialization, control, and readout are performed using voltage pulses on gate electrodes. Initialization is typically achieved by aligning the $|\downarrow\rangle$ state below the reservoir Fermi level, allowing rapid relaxation into this state. Coherent control then proceeds via ESR pulses, inducing spin rotations with Rabi frequencies up to tens of MHz. Readout is accomplished through spin-dependent tunneling: after a final rotation aligning the spin

state with the measurement axis, the $|\uparrow\rangle$ state is energetically aligned with the reservoir. When the spin of the measured qubit is antiparallel to the reservoir (or SET) spin, tunneling into the reservoir is allowed, resulting in a detectable change in charge sensed by a nearby quantum point contact (QPC) or single-electron transistor (SET). Conversely, if the spins are parallel, tunneling is forbidden due to the Pauli exclusion principle, and no charge transition is observed.

The Si-MOS platform benefits from the natural abundance of spin-zero $^{28}$Si nuclei, with further isotopic enrichment suppressing decoherence from nuclear spin noise. Typical $T_2^*$ times in purified $^{28}$Si exceed tens of microseconds, with Hahn-echo coherence times $T_2$ surpassing 10 ms and energy relaxation times approaching 1 s under optimal conditions [26]. A key material-specific challenge in Si-MOS is valley degeneracy, where electrons occupy multiple conduction band minima. However, vertical confinement and strong electric fields in modern devices achieve valley splittings above 0.8 meV, sufficient to suppress leakage into excited valley states [27].

Recent advances in gate-stack engineering, including multi-layer overlapping gates, have enabled precise definition of confinement potentials and enhanced tunability compared to earlier single-layer "stadium" geometries. Combined with the larger effective mass of silicon (requiring $\sim 50\,\text{nm}$ dots), these advances have led to qubit control with exceptional performance. ESR-based single-qubit gate fidelities have reached the sub-percent level using optimal pulse shaping [28]. High-fidelity readout $> 99\%$ with millisecond-scale integration times [29] positions Si-MOS spin qubits as a leading platform for scalable quantum computing.

### 1.2.4 Two-qubit Gates via Exchange Coupling

Entangling two-qubit gates in silicon quantum dot systems are realized through the exchange interaction between neighboring electron spins. When two electrons occupy adjacent quantum dots in the $(1, 1)$ charge configuration, their spins interact via the Heisenberg exchange Hamiltonian [23]:

$$\hat{H}_{\text{ex}} = J(t)\,\mathbf{S}_1 \cdot \mathbf{S}_2, \tag{1.8}$$

where $J(t)$ is the tunable exchange coupling strength and $\mathbf{S}_i = (S_{ix}, S_{iy}, S_{iz})$ is the spin operator of electron $i$. Explicitly, the scalar product expands as:

$$\mathbf{S}_1 \cdot \mathbf{S}_2 = S_{1x}S_{2x} + S_{1y}S_{2y} + S_{1z}S_{2z}, \tag{1.9}$$

The time evolution operator under this Hamiltonian is:

$$U(t) = \exp\left(-i\frac{Jt}{\hbar}\,\mathbf{S}_1 \cdot \mathbf{S}_2\right), \tag{1.10}$$

where $t$ is the interaction duration. By tuning $J$ and $t$, various two-qubit gates can be implemented:

- For $Jt/\hbar = \pi$, $U(t)$ corresponds to the full SWAP gate:

$$\text{SWAP} = \begin{pmatrix} 1 & 0 & 0 & 0 \\ 0 & 0 & 1 & 0 \\ 0 & 1 & 0 & 0 \\ 0 & 0 & 0 & 1 \end{pmatrix},$$

  which exchanges the spin states of the two qubits.

- For $Jt/\hbar = \pi/2$, $U(t)$ realizes the $\sqrt{\text{SWAP}}$ gate:

$$\sqrt{\text{SWAP}} = \begin{pmatrix} 1 & 0 & 0 & 0 \\ 0 & \frac{1}{2}(1+i) & \frac{1}{2}(1-i) & 0 \\ 0 & \frac{1}{2}(1-i) & \frac{1}{2}(1+i) & 0 \\ 0 & 0 & 0 & 1 \end{pmatrix},$$

  which partially exchanges the spins and generates entanglement.

Control over $J$ is achieved electrically by tuning the interdot tunnel coupling $t_c$ and detuning $\varepsilon$ between the two quantum dots, as described in Sec. 1.2.2. The ability to switch $J$ on and off with gate voltages enables fast, high-fidelity two-qubit gates compatible with large-scale arrays of silicon spin qubits. Recent experiments have demonstrated exchange-based two-qubit gates with fidelities exceeding 99% [30].

## 1.3 Key Challenges

### 1.3.1 Gate Miscalibration in Quantum Dot Systems

Precise electrostatic control is essential for the reliable operation of quantum dot qubits. In practical devices, however, the voltages applied to gate electrodes are often subject to

systematic, static deviations from their intended values. Even when experimentalists believe they are applying well-calibrated voltages, imperfections in the control hardware and long-term drifts can cause the actual electrostatic potential experienced by the quantum dot to differ from the target configuration. This phenomenon, commonly referred to as *gate miscalibration*, represents a persistent offset in the average electric potential landscape and constitutes a significant source of control error in spin qubit systems.

Gate miscalibration can arise from various sources. These include gain and offset errors in voltage sources, imperfect knowledge of the gate-to-dot transfer functions, cross-capacitance and screening effects from neighboring electrodes, and fabrication-induced disorder in the material environment. As a result, nominally identical voltage pulses can yield different qubit responses, depending on the specific device and context. These discrepancies can shift the operating point of the qubit away from its calibrated setting, altering quantities such as tunnel rates, exchange coupling, or resonance frequencies, and ultimately degrading gate fidelity.

Importantly, even small systematic deviations in control voltages can induce significant errors over many gate operations, particularly in algorithms requiring high-precision pulse sequences or repeated calibrations.

In addition to such static miscalibrations, quantum dot systems also exhibit time-dependent instabilities, often grouped under the term *calibration drift* [31]. These include gradual relaxation following thermal cycling, sudden telegraphic jumps due to charge rearrangements, and low-frequency fluctuations in the electrostatic environment. While drift presents distinct challenges for long-term stability, this work focuses primarily on static voltage miscalibration as a dominant and experimentally relevant source of qubit control error.

Understanding and mitigating the effects of gate miscalibration is essential for developing scalable, high-fidelity quantum processors based on silicon quantum dots. This motivates the need for robust control protocols and systematic analysis of calibration-related errors, which we explore through simulations in the chapters that follow.

### 1.3.2 The Challenge of Charge Noise in Spin Qubits

Charge noise has emerged as another major factor limiting the performance of silicon spin qubits. Despite its recognized impact on qubit coherence, the microscopic origins of charge noise in gate-defined quantum dot architectures are still not fully understood [32]. It is generally attributed to a combination of microscopic charge traps, interface defects, and mobile impurities within dielectric layers and at heterointerfaces such as $Si/SiO_2$ and

Si/SiGe. As these charge fluctuators stochastically switch between metastable states, they produce time-dependent local electric fields at the qubit site.

Charge noise refers to random fluctuations of electric fields in the vicinity of a spin qubit. Although an isolated electron spin does not couple directly to electric fields, silicon quantum dot architectures exhibit spin-to-charge coupling mediated by spin–orbit interaction at heterointerfaces [17]. This coupling allows electric field fluctuations to modulate the effective electron $g$-factor, leading to variations in the Zeeman splitting, and generate effective magnetic field noise through gradients in the external magnetic field. As a result, charge noise can cause both dephasing and relaxation of spin qubits, degrading coherence parameters such as $T_1$, $T_2^*$, and $T_2$.

In addition, charge noise perturbs the electrostatic confinement potential, shifting the local chemical potential $\mu$. Since both the $g$-factor ($\delta g$) and the exchange interaction $J(V)$ depend sensitively on the electrostatic environment, such perturbations induce temporal fluctuations in these parameters, further reducing qubit fidelity.

Experimentally, the power spectral density (PSD) of charge noise in silicon quantum dots exhibits a characteristic $1/f^\alpha$ dependence over an exceptionally broad frequency range—from millihertz up to megahertz and beyond [32]. This spectral behavior reflects the contributions of a large ensemble of two-level fluctuators (TLFs), each representing a localized charge trap that randomly switches between two metastable charge configurations. When the switching rates of these fluctuators are distributed approximately log-uniformly, their combined noise spectrum naturally produces the emergent $1/f^\alpha$ behavior with $\alpha \approx 1$. Measurements in Si/SiGe and Si-MOS devices reveal that the typical amplitude of charge-induced energy fluctuations at $f = 1\,\mathrm{Hz}$ falls in the range $A_\mu = 0.1\text{–}10\,\mu\mathrm{eV}/\sqrt{\mathrm{Hz}}$ [33, 34]. This corresponds to a chemical potential noise spectral density $S_\mu(f) = A_\mu^2(1\,\mathrm{Hz}/f)$.

To mitigate these detrimental effects, device operation at "sweet spots" where the first-order voltage sensitivity $\partial J/\partial V$ vanishes has proven effective in suppressing the impact of charge noise. Additionally, dynamical decoupling pulse sequences filter out low-frequency noise components, prolonging coherence times and enabling spectral characterization of the noise [35].

In this thesis, we model the effect of charge fluctuations with the gate voltage noise, enabling their impact on exchange interactions to be quantified through the sensitivity $\partial J/\partial V$ and allowing realistic simulations of their stochastic nature and broad frequency content using ensembles of random telegraph signals (RTS). This approach provides a framework for exploring potential noise mitigation strategies.

# Chapter 2

# Methods

## 2.1 Spin Qubit Simulator

Our group has developed a versatile simulator to model the dynamics of spin qubits in realistic silicon quantum dot (QD) devices. The tool implements a full-stack computational pipeline, beginning with three-dimensional electrostatic simulations using a finite-element Poisson solver [36], in which gate voltages are systematically varied. The resulting electrostatic potential and electric field profiles are post-processed to extract two-dimensional horizontal slices at the expected position of the two-dimensional electron gas (2DEG) beneath the $Si/SiO_2$ interface.

These interpolated 2D potentials define the confining landscape for gate-defined QDs and serve as inputs to solve the two-dimensional single-particle Schrödinger equation. A masking procedure isolates individual dot or dot-pair potentials, for which single-particle ground state wavefunctions (SPGSWs) are calculated. These wavefunctions are then used to estimate effective parameters such as the electron $g$-factor via Stark shift models and interdot exchange coupling via Heitler-London or Hund-Mulliken approximations. These parameters exhibit strong dependence on gate voltages and capture the nonlinear response of spin qubit systems to electrostatic control.

The simulator constructs an effective spin Hamiltonian incorporating voltage-tunable

Zeeman and exchange interactions, expressed as [37]

$$H = \frac{\mu_B B_z}{\hbar} \sum_{j=1}^{N} \frac{g_j\left(\vec{V}(t), \vec{W}(t)\right) - g_0}{2} Z_j - \frac{\omega_{\mathrm{RF}}(t) - \omega_{\mathrm{RF}}^{(0)}}{2} \sum_{j=1}^{N} Z_j + B_{\mathrm{RF}}(t) \left\{ \cos\phi(t) \sum_{j=1}^{N} \frac{\mu_B}{\hbar} X_j + \sin\phi(t) \sum_{j=1}^{N} \frac{\mu_B}{\hbar} Y_j \right\} + \sum_{j=1}^{N-1} J_j\left(\vec{V}(t), \vec{W}(t)\right) \frac{\vec{\sigma}_j \cdot \vec{\sigma}_{j+1}}{4\hbar}, \quad (2.1)$$

where

- $\mu_B$ is the Bohr magneton;
- $B_z$ and $B_{\mathrm{RF}}(t)$ are the static Zeeman field and the envelope of the ESR field (in tesla), respectively;
- $\omega_{\mathrm{RF}}(t) = 2\pi f_{\mathrm{RF}}(t)$ and $\phi(t)$ are the time-dependent ESR field frequency (radio-frequency range) and phase;
- $J_{j,j+1}(t)$ is the voltage-controlled exchange coupling between the $j^{\mathrm{th}}$ and $(j+1)^{\mathrm{th}}$ dots (in joules);
- $\vec{\sigma}_j = \{X_j, Y_j, Z_j\}$ is the Pauli vector of the $j^{\mathrm{th}}$ spin;
- $g_j(t)$ is the voltage-controlled in-plane $g$-factor of the $j^{\mathrm{th}}$ spin. The out-of-plane $g$-factor is set to 2.

Here, $g_0$ is the idling $g$-factor, defined as the value of $g_j$ at a voltage configuration $\vec{V}_0, \vec{W}_0$ deeply within the charge stability region where all qubits share an identical $g$-factor, and $\omega_{\mathrm{RF}}^{(0)} = g_0 \mu_{\mathrm{B}} B_z / \hbar$ is the corresponding idling ESR frequency, serving as the reference frame for spin rotations.

Control inputs such as global ESR fields, local gate voltages, and their time dependence are mapped to the Hamiltonian coefficients. This enables simulations of spin dynamics via time evolution under the Lindblad master equation formalism, including relaxation and dephasing effects.

Our software also features a custom control pulse design routine for voltages and ESR magnetic fields, automatically accounting for cross-coupling between quantum dots and ensuring perfect theoretical unitary fidelity. The algorithm relies on designing a time-ordered spin Hamiltonian $H = H_0 S(t)/T$ as described in [38], where $H_0$ is a time-independent generator of a quantum logic gate, $S(t)$ is a smooth shape function, and $T$ is the pulse length. This enables us to design arbitrary rotations in the global ESR field, $\mathrm{SWAP}^{k/2}$, and $\mathrm{CPHASE}(\alpha)$ gates. Voltage pulses $\vec{V}(t)$ are reverse-engineered from the $g$-factor and exchange pulses by solving a custom system of ODEs for $V(S)$ and composing them with the chosen shape of the spin Hamiltonian $S(t)$.

The simulator also supports determination of Hubbard model [39] parameters—chemical potential, tunnel coupling, and Coulomb terms—allowing cross-verification of spin and charge dynamics within the same architecture. This comprehensive modeling framework facilitates the design, calibration, and benchmarking of multi-qubit gate operations, and supports integration of quantum algorithm simulations within realistic silicon QD device architectures.

In all simulations presented in this thesis, the spin relaxation and dephasing times are set to infinity ($T_1, T_2 \to \infty$) within the simulator, effectively neglecting these processes.

## 2.2 Modeling Charge Noise via Random Telegraph Noise

In Chapter 1, we discussed how charge noise, with a characteristic $1/f$-like power spectral density, is a leading source of spin qubit dephasing in solid-state silicon devices. A widely used approach to emulate such $1/f$ noise is to model it as an ensemble of Random Telegraph Noise (RTN) sources, two-level fluctuators with a wide distribution of switching rates, that collectively reproduce the spectral profile $1/f$ [40, 41]. In this section, we describe how we implement RTN in our simulator and explain how the resulting charge fluctuations are incorporated into the quantum system to assess their impact on coherence and gate fidelity.

RTN can be explained by the stochastic trapping and detrapping of charge carriers at localized defect sites. Each RTN source produces a two-level signal with discrete switching between a high- and a low-state state, where the transitions are governed by a Poisson process. The characteristics of such noise are illustrated in Fig. 2.1. Panel (a) shows a typical time-domain trace of a single RTN realization with amplitude $A = 1\,\mathrm{mV}$ and symmetric average lifetimes $\langle \tau_0 \rangle = \langle \tau_1 \rangle = 100\,\mathrm{ns}$. Panel (b) presents the corresponding power spectral density (PSD) averaged over multiple realizations. In the low-frequency regime

($f \ll f_c$), the power spectral density (PSD) approaches a constant value, corresponding to quasistatic fluctuations. The transition to the high-frequency regime is characterized by a Lorentzian roll-off beyond the cutoff frequency $f_c = (2\pi\tau)^{-1}$ [42], where the PSD decays as $1/f^2$. For $f \gg f_c$, the rapidly varying noise components are effectively averaged out by qubit operations, reducing their impact on coherence.

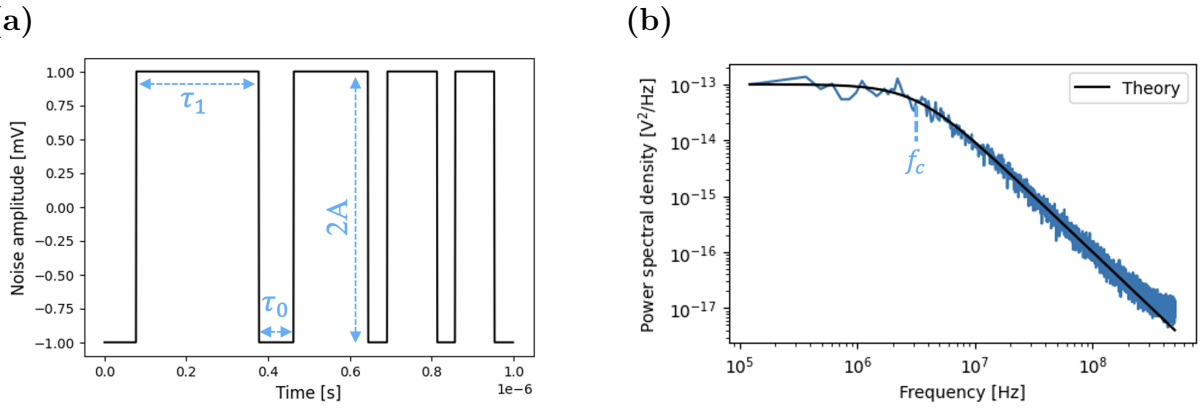



Figure 2.1: Characteristics of random telegraph noise. **(a)** Time-domain trace of a single RTN realization with amplitude $A = 1\,\text{mV}$ and symmetric switching time $\langle\tau_0\rangle = \langle\tau_1\rangle = 100\,\text{ns}$. **(b)** Power spectral density (PSD) from 20 summed and normalized RTN realizations with the same parameters as in (a). The black line shows the theoretical Lorentzian PSD with $1/f^2$ decay at high frequencies. The blue dashed line indicates the cutoff frequency $f_c$.

The PSD of a single RTN process can be expressed as

$$S_{RTN}(f) = \frac{4A^2\tau}{1 + (2\pi f\tau)^2}, \tag{2.2}$$

where $A$ is the noise amplitude and $\tau$ is the average switching time (assuming $\tau_0 = \tau_1 = \tau$ for simplicity).

Building on the description of RTN, we now consider the collective behavior of many independent RTN sources and their ability to generate $1/f$-like spectra observed in solid state devices. It is well established that an ensemble of two-level fluctuators with a broad distribution of switching times can reproduce the characteristic power spectral density $1/f$ [43].

When a large number of such RTN sources are combined, the total PSD is obtained by integrating over a distribution of switching times $p(\tau)$:

$$S_{\text{total}}(f) = \int_{\tau_{\min}}^{\tau_{\max}} S_{\text{RTN}}(f, \tau)\, p(\tau)\, d\tau. \tag{2.3}$$

If the switching times are log-uniformly distributed: $p(\tau) \propto 1/\tau, \tau \in [\tau_{\min}, \tau_{\max}]$, which corresponds physically to a uniform density of charge traps in the oxide layer with exponentially distributed activation energies [40], the integral yields

$$S_{\text{total}}(f) \propto \frac{1}{f}, \tag{2.4}$$

over a wide intermediate frequency range where $\tau_{\min}^{-1} \ll f \ll \tau_{\max}^{-1}$.

This result provides an explanation for the emergence of $1/f$ noise in solid-state systems: a dense spectrum of two-level fluctuators with logarithmically distributed time scales naturally reproduces the observed power-law behavior in the frequency domain.

To generate RTN signals with the desired statistical properties, we implement a numerical routine that constructs time-domain traces of specified duration. The routine accepts as input the noise amplitude $A$, total noise duration time $T$, sampling period $s$, and characteristic switching time $\tau$. Segment lengths are sampled from an exponential distribution with $\tau$, reflecting the Poissonian nature of the switching events. These segment durations are cumulatively summed to determine the switching times, and the process is repeated until the total duration exceeds $T$. The resulting piecewise-constant signal alternates between $+A$ and $-A$ at each switching event, with the initial state randomly assigned to $+A$ or $-A$ with equal probability. Finally, the continuous trace is discretized at intervals of $s$ to produce a time series compatible with the simulator's integration routines. This procedure is used to generate the RTN signals illustrated in Fig. 2.1.

Following the description of our RTN generation routine, we analyze the spectral characteristics of the simulated traces to assess how the switching time $\tau$ influences their frequency content. As shown in Fig. 2.2, RTN sequences exhibit spectral features determined by $\tau$.

In our simulation, the duration of all quantum gates is set to $10\,\mu$s, corresponding to an operational frequency $f_g = 100\,$kHz. The influence of RTN on gate fidelity is hypothesized to depend on the noise correlation time $\tau$, due to the matching or mismatching of noise fluctuations with gate operation timescales.

For very short $\tau$ (high-frequency RTN), rapid switching events are expected to average out over the duration of individual gates, leading to a relatively small net effect on the

qubit dynamics. At the other extreme, for very long $\tau$ (low-frequency RTN), the noise acts approximately as a static offset during each gate operation, and its impact is mainly determined by the amplitude of this offset.

Figure 2.2 illustrates how varying $\tau$ shifts the spectral knee across frequency bands. Short $\tau$ values push $f_c$ into the MHz regime, resulting in fast noise that can be dynamically averaged out. However, as $\tau$ increases, the noise spectrum shifts towards lower frequencies. Any noise with frequency below $1/t_{\text{experiment}}$ effectively becomes invisible during the experiment and cannot be mitigated by dynamical decoupling or other control techniques. Consequently, low-frequency noise poses the most significant threat to gate fidelity.

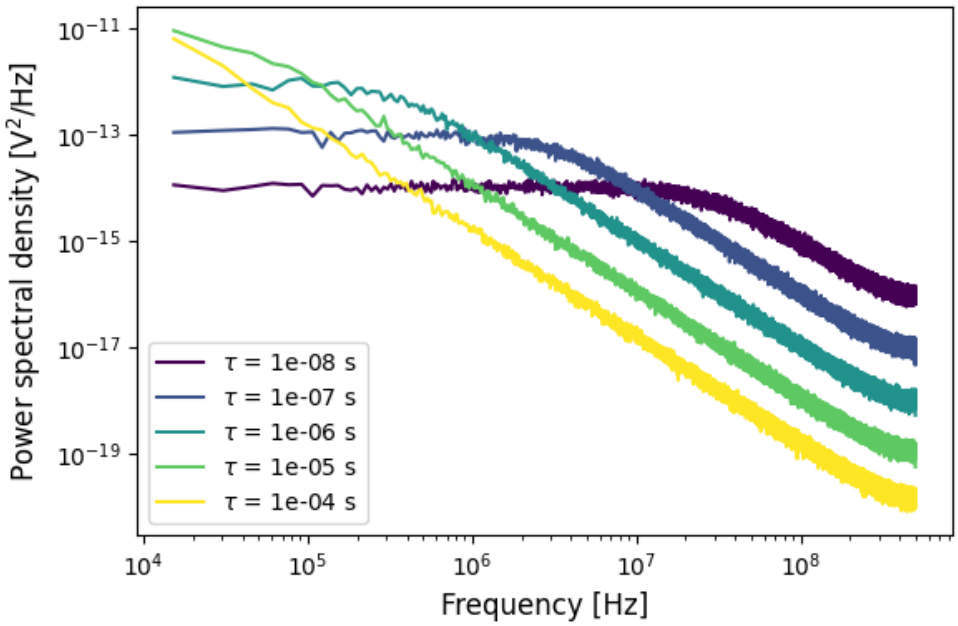



Figure 2.2: Power spectral densities (PSDs) of RTN traces generated with fixed amplitude $A = 1\,\text{mV}$ and varying switching times $\tau$. Each curve shows the PSD from 50 summed and normalized RTN realizations for $\tau = \tau_0 = \tau_1 \in \{10^{-8}, 10^{-7}, 10^{-6}, 10^{-5}, 10^{-4}\}\,\text{s}$. Increasing $\tau$ shifts the cutoff frequency $f_c = (2\pi\tau)^{-1}$ to lower values, illustrating the transition from fast to quasistatic noise.

The next step is to integrate these fluctuations into the qubit control by superimposing them on the ideal gate voltage profiles. For each electrode, 50 independent RTN sequences are generated and summed together. The resulting signal is then normalized to match the power spectrum of a single RTN trace. This procedure ensures that each electrode receives

an independent effective noise signal while maintaining consistent spectral characteristics across all plunger and barrier gates.

This approach is motivated by the fact that key spin qubit parameters in silicon devices are intrinsically sensitive to variations in the electrostatic environment. The electron $g$-factors depend approximately linearly on the local potential, while the interdot exchange coupling $J$ exhibits a highly nonlinear response. By directly perturbing the gate voltages with RTN sequences, we induce fluctuations in these effective Hamiltonian parameters in a physically consistent manner. This reflects the reality that charge noise couples to qubits predominantly through its modulation of the electrostatic landscape, thereby altering spin splittings and exchange interactions.

Figure 2.3 illustrates this procedure for a SWAP gate of duration $T = 10\,\mu$s. The left panel shows the ideal control pulses applied to electrodes $V_1, V_2$, and $W_1$, while the right panel displays the same pulses after superimposing RTN with parameters amplitude $A = 2\,$mV and switching time $\tau = 100\,$ns.

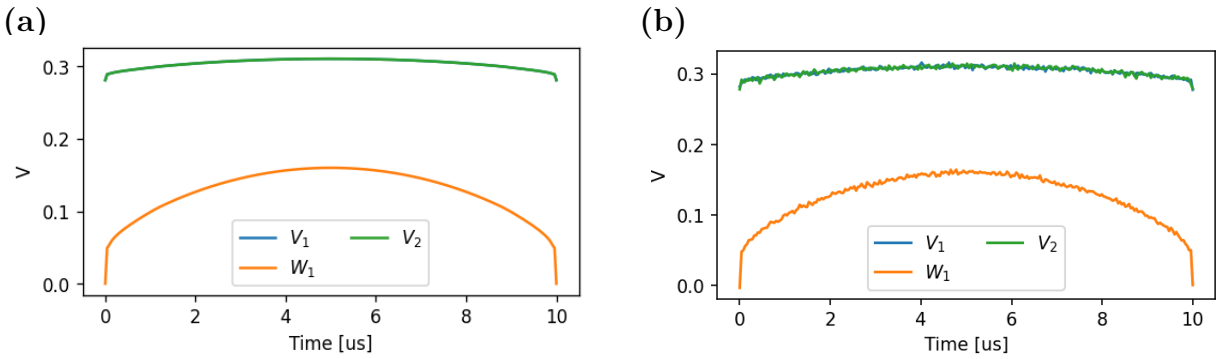



Figure 2.3: Comparison of SWAP gate voltage waveforms with and without simulated charge noise. The noise is generated by summing 50 independent RTN traces per electrode and normalizing to preserve the spectral profile, then added directly to the ideal control pulses. The pulse uses a wide Gaussian envelope with a total duration of $10\,\mu$s. (a) Ideal gate voltage. (b) Gate voltages with a superimposed noise sequence ($A = 2\,$mV, $\tau = 100\,$ns).

## 2.3 Quantum Process Tomography

Quantum tomography serves as a cornerstone of quantum characterization, verification, and validation, which is indispensable for the fabrication and development of quantum computers. The foundational tomography techniques—including quantum state tomography (QST), Quantum Process Tomography (QPT), gate set tomography, process tensor tomography, and interleaved sequence tomography—provide the basis for a wide array of applications, from device calibration [44, 45, 46] to quantum error mitigation [47] and quantum error correction [48].

The tomography first emerged under the assumption that the experimenter possesses full knowledge of the quantum gates and measurements. By preparing a tomographically complete basis set, one can reconstruct the unknown quantum state from the observed probabilities. Building on this framework, QPT generalizes the methodology to reconstruct the dynamics of a black-box quantum process. The goal of QPT is to determine an unknown completely positive (CP) map $\mathcal{E} \in \mathcal{B}(\mathcal{H}_d)$, where $\mathcal{B}(\cdot)$ denotes the space of bounded linear operators on the Hilbert space $\mathcal{H}_d$ [49].

These tomography protocols have become foundational tools in experimental quantum computing, underpinning not only device characterization but also the development of advanced error mitigation and correction strategies. In our simulator, to systematically characterize the influence of noise on quantum gate operations, we employ QPT as a diagnostic tool.

Formally, $\mathcal{E}$ maps an input density matrix $\rho_{\text{in}}$ to an output density matrix $\rho_{\text{out}}$, which can be expressed via the Kraus operator sum representation [50]:

$$\mathcal{E}(\rho) = \sum_i E_i \rho E_i^\dagger, \tag{2.5}$$

where the Kraus operators $\{E_i\}$ satisfy the trace-preserving condition $\sum_i E_i^\dagger E_i = I$. These operators can in turn be expanded over a fixed, complete basis $\{\tilde{E}_m\}$ as:

$$\begin{aligned} E_i &= \sum_m e_{im} \tilde{E}_m, \\ \mathcal{E}(\rho) &= \sum_{m,n} \chi_{mn} \tilde{E}_m \rho \tilde{E}_n^\dagger, \end{aligned} \tag{2.6}$$

where $\chi$ is the process matrix (also called the Chi matrix), a positive semidefinite Hermitian matrix that fully characterizes the quantum process.

The Standard Quantum Process Tomography (SQPT) procedure is illustrated schematically in Fig. 2.4. It involves preparing a complete set of $d^2$ linearly independent input states $\{\rho_i\}$, passing each through the process $\mathcal{E}$, and performing quantum state tomography on the resulting outputs. Here, we adopt the standard Liouville space notation, where density matrices $\rho_i$ are vectorized as $|\rho_i\rangle\rangle$ in a $d^2$-dimensional Hilbert–Schmidt space, allowing quantum processes $\mathcal{E}$ to be represented as linear superoperators acting on these vectors. Given the observed measurement probabilities

$$p_{ij} = \langle\langle M_j|\mathcal{E}|\rho_i\rangle\rangle,$$

where $M_j$ are measurement operators spanning $\mathcal{H}_d$, one can reconstruct the process matrix $\chi$ by solving a linear system.

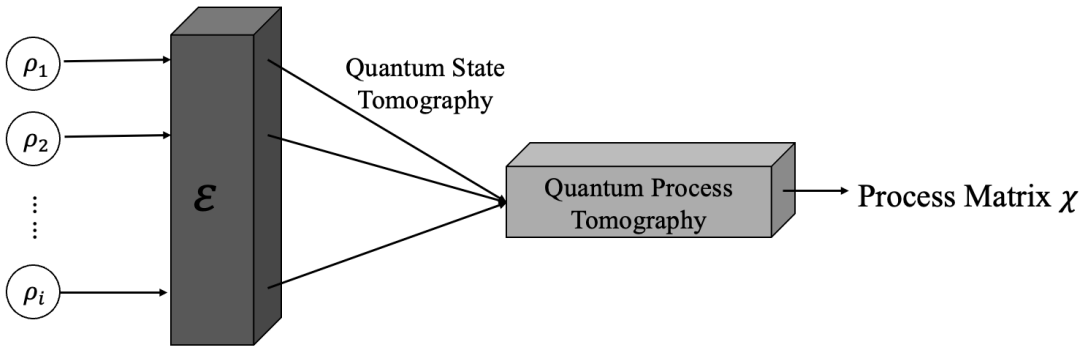



Figure 2.4: Schematic of SQPT. A complete set of linearly independent input states $\rho_i$ is prepared and passed through the unknown quantum process $\mathcal{E}$. The resulting output states are measured using quantum state tomography, enabling reconstruction of the process matrix $\chi$.

In our two-qubit simulations, the complete set comprises 16 input states, constructed from tensor products of Pauli operators applied to the initial state $|00\rangle$:

$$\rho_{nm} = T_n|00\rangle\langle 00|T_m^\dagger,$$

where $T_n \in \{I \otimes I, I \otimes X, X \otimes I, X \otimes X\}$, and $I$, $X$ denote the identity and Pauli-X matrices, respectively. Each of these input states is propagated through the noisy process, and the corresponding output states are measured to reconstruct $\chi$.

Mathematically, assuming $\mathcal{E}(\rho_j) = \sum_k \lambda_{jk}\rho_k$, and noting that

$$\tilde{E}_m\rho_j\tilde{E}_n^\dagger = \sum_k \beta_{jk}^{mn}\rho_k, \tag{2.7}$$

we relate the coefficients through:

$$\sum_{m,n} \chi_{mn} \beta_{jk}^{mn} = \lambda_{jk}. \tag{2.8}$$

By reshaping $\chi$ and $\lambda$ into vectors and $\beta$ into a $d^4 \times d^4$ matrix, this system becomes:

$$\beta\chi = \lambda.$$

In experimental QPT, directly inverting this system often yields unphysical $\chi$-matrices due to statistical noise, SPAM errors, and the fact that each run of the process may experience different realizations of environmental noise. To ensure physical validity, convex constraint optimization (CCO) [51] is commonly employed, formulating the reconstruction as a semidefinite program (SDP):

$$\min_{\chi} \|\beta\chi - \lambda\|^2 \quad \text{s.t.} \quad \chi \geq 0, \ \sum_{m,n} \chi_{mn} \tilde{E}_n^\dagger \tilde{E}_m = I, \tag{2.9}$$

where the constraints enforce complete positivity and trace preservation (CPTP).

In contrast, our simulator avoids this complication. Since we generate and apply the same set of noise sequences to all 16 input states of each two-qubit gate, the process remains consistent across all tomography experiments. This deterministic noise environment eliminates the random variations that necessitate CCO in experimental settings, allowing us to directly solve for a physically valid $\chi$-matrix.

### 2.3.1 Error Process Matrix and Kraus Representation

Building on the reconstructed process matrix $\chi$ from QPT, we now turn to analyzing the noise-induced deviations in quantum gates beyond simple fidelity results. This analysis offers a finer-grained view of error types and their physical origins, enabling us to distinguish, to a large extent, between coherent control imperfections and incoherent noise contributions.

A central quantity in this analysis is the *error process matrix*, $\chi^{\text{err}}$, which isolates the contribution of noise from the intended ideal gate operation [52]. It is defined via a transformed quantum channel:

$$\rho_{\text{final}} = \sum_{m,n} \chi_{mn}^{\text{err}} \, \tilde{E}_m \, U \, \rho_{\text{in}} \, U^\dagger \, \tilde{E}_n^\dagger, \tag{2.10}$$

where $U$ is the target (ideal) unitary gate and $\tilde{E}_m$ are the Pauli basis operators (consistent with Equation 2.6). This formulation effectively factors out the intended evolution $U$, leaving behind a residual process that captures all deviations due to noise and control imperfections.

In the noiseless limit, the error process reduces to the identity channel:

$$\chi^{\text{err}}_{mn} = \delta_{m0}\,\delta_{n0}, \quad \text{i.e.,} \quad \chi^{\text{err}}_{00} = 1, \tag{2.11}$$

where $\chi^{\text{err}}_{00}$ directly quantifies the fidelity of the process, and non-zero off-diagonal terms reveal specific error channels introduced by the environment.

Beyond the error process matrix, we also extract the *Kraus operator representation* of the process. This provides a complementary perspective by expressing the quantum operation as an operator-sum decomposition:

$$\mathcal{E}(\rho) = \sum_i K_i \rho K_i^\dagger, \tag{2.12}$$

where each Kraus operator $K_i$ can be obtained from the eigen-decomposition of $\chi$:

$$\chi = U D U^\dagger, \quad D = \text{diag}(d_1, d_2, \dots), \tag{2.13}$$

$$K_i = \sqrt{d_i} \sum_j U_{ji}\,\tilde{E}_j. \tag{2.14}$$

This representation provides physical insight into the dominant decoherence mechanisms affecting the system.

As an illustration, we perform QPT on a noisy implementation of the $R_x(\pi/2)$ gate applied to qubit 1 while the 2nd qubit is performing a non-resonant $2\pi$ rotation. Figure 2.5 shows the resulting error process matrices: This visualization highlights how noise redistributes weight into components of $\chi^{\text{err}}$, revealing both coherent and incoherent error channels introduced by the RTN perturbations.

### 2.3.2 Unitary Error

Extending to the Kraus operator decomposition, we observe that under mild noise conditions, a single Kraus operator—typically associated with the largest eigenvalue of the process matrix $\chi$—dominates the system dynamics. This operator, denoted as $K_{\text{dom}}$, approximately captures the coherent component of the noisy quantum process, incorporating both the intended unitary gate $U$ and leading-order coherent noise.

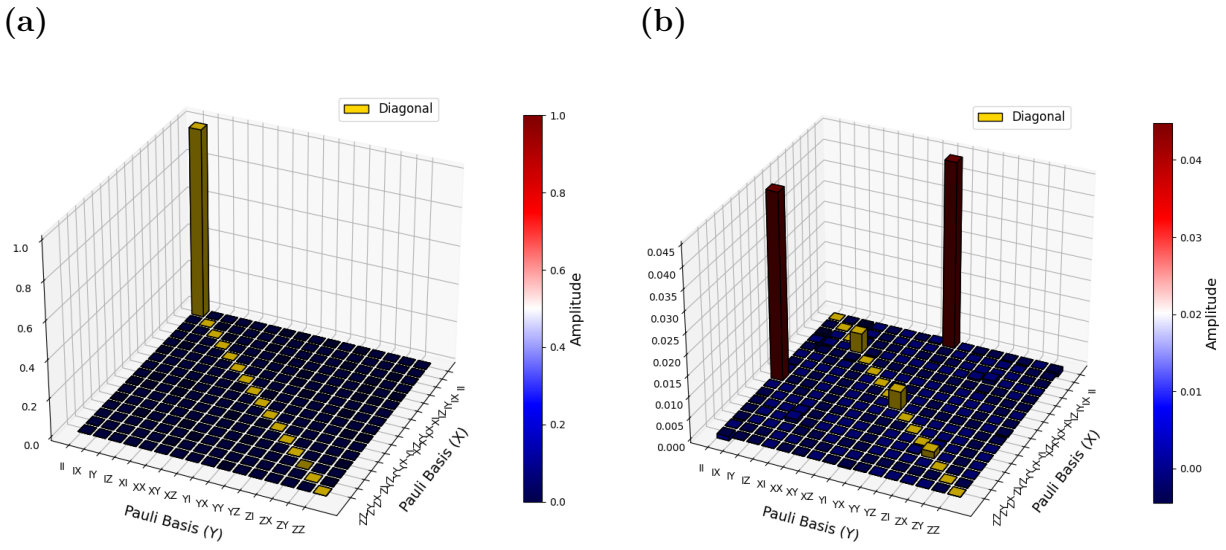



Figure 2.5: Error process matrices $\chi^{\text{err}}$ for the $RX(\pi/2)$ gate on qubit 1. Color bars indicate matrix element amplitudes in the Pauli basis. (a) Ideal case ($\chi^{\text{err}}_{00} = 1$) showing no noise. (b) RTN noise with amplitude $3.5 \times 10^{-3}\,\text{V}$ and $\tau = 1\,\mu\text{s}$, averaged over 100 realizations. For clarity, $\chi^{\text{err}}_{00}$ is set to zero.

To isolate the unitary component of the noise, we first remove the contribution of the ideal gate from $K_{\text{dom}}$ by defining a residual operator:

$$K_{\text{res}} = U^{\dagger} K_{\text{dom}}. \tag{2.15}$$

This step effectively undoes the ideal unitary evolution, leaving a residual operator $K_{\text{res}}$ that encodes only the deviations introduced by noise.

Since $K_{\text{res}}$ is not guaranteed to be unitary, we project it onto the nearest unitary operator. To this end, we define an effective Hamiltonian $H_{\text{err}}$ via a Hermitian projection of the matrix logarithm:

$$H_{\text{err}} = \frac{i \log(K_{\text{res}}) - (i \log(K_{\text{res}}))^{\dagger}}{2}, \tag{2.16}$$

where $\log(\cdot)$ denotes the matrix logarithm. This procedure ensures that $H_{\text{err}}$ is Hermitian, corresponding to a physically meaningful generator of unitary evolution.

The approximate unitary error operator is given by the following:

$$U_{\text{err}} = e^{-iH_{\text{err}}}. \tag{2.17}$$

Finally, the corrected output state can be expressed as:

$$\rho_{\text{corrected}} = U_{\text{err}}^{\dagger} \rho_{\text{final}} U_{\text{err}}, \tag{2.18}$$

where $\rho_{\text{final}}$ denotes the noisy output state obtained in the presence of noise.

This procedure systematically extracts the leading-order coherent error and provides a means to suppress it.

# Chapter 3

# Effects of noise on quantum gate operations

## 3.1 Impact of Voltage Miscalibration on Gate Fidelity

With the methods established in the previous chapter—including the quantum dot simulator, charge noise modeling, and QPT—we begin our results by quantifying how voltage miscalibration affects quantum gate performance. This analysis provides an essential baseline for understanding more complex noise sources, such as RTN, in subsequent sections.

We simulate the effect of voltage miscalibration using a Python-based simulator mentioned previously in Sec. 2.1. Control miscalibration is modeled by introducing stochastic multiplicative and additive errors to the applied voltage waveforms:

$$V'(t) - V_{\text{idle}} = a \cdot (V(t) - V_{\text{idle}}) + b, \tag{3.1}$$

where $V(t)$ is the ideal control voltage waveform, $V'(t)$ is the miscalibrated waveform, and $V_{\text{idle}}$ represents the voltage setting corresponding to the qubits' idling configuration. The idling state is defined as the operating point where no active pulses are applied, ensuring the qubits remain within their charge stability regime without inducing unintended dynamics. At $V_{\text{idle}}$, parameters such as the electron spin resonance (ESR) field ($\Omega = 0$) and g-factor deviation ($\delta g_j = \delta g_0$) are chosen so that all qubits are decoupled from control fields and share a common idle condition. This formulation ensures that the stochastic offset $b$ perturbs only the active part of the waveform while preserving the system's reference point. The multiplicative factor $a$ and additive offset $b$ are sampled from Gaussian distributions

with $\mathbb{E}[a] = 1$, $\mathbb{E}[b] = 0$, and standard deviations $\sigma_a$ and $\sigma_b$, respectively. This error model captures realistic imperfections arising from waveform distortion, amplifier drift, and environmental instability.

We simulate the gate fidelity for four representative quantum operations in a two-qubit quantum dot system:

- $R_X(\pi/2)$: a single-qubit rotation by angle $\pi/2$ about the $X$-axis applied to qubit 1, while qubit 2 undergoes an idle $2\pi$ rotation;
- Hadamard: a single-qubit $\pi$-rotation around the $(1, 0, 1)$ axis applied to qubit 2, with qubit 1 simultaneously undergoing an idle $2\pi$ rotation;
- Controlled-Z gate (CZ): a two-qubit entangling gate implemented via combined control of the qubit frequency deviation and the isotropic exchange interaction [53];
- $\sqrt{\text{SWAP}}$: a two-qubit partial swap gate.

Each gate is implemented using Gaussian-shaped pulses of 10 $\mu$s duration, with independent stochastic samples of $(a, b)$ applied to each of the three voltage channels $(V_1, V_2, W)$. For each noise setting $(\sigma_a, \sigma_b)$, the process fidelity is computed over 800 independent realizations using:

$$F = \frac{d \cdot \left|\frac{1}{d^2} \operatorname{Tr}(U^\dagger U')\right| + 1}{d + 1},$$

where $U$ and $U'$ are the ideal and noisy unitary operators, and $d$ is the dimension of the Hilbert space.

To quantify variability across noise realizations, error bars are added to each data point in Fig. 3.1. These error bars represent the spread of the cumulative distribution function (CDF) of the simulated fidelities: for each parameter setting, the $20^{\text{th}}$ and $80^{\text{th}}$ percentiles of the CDF are computed, and the resulting range is used as the error interval. This percentile-based approach provides a robust measure of the central 60% spread of fidelity values, effectively capturing the stochastic variation without being overly sensitive to outliers.

Figure 3.1 shows the log-scaled infidelity $\log_{10}(1 - F)$ as a function of $\sigma_b$ for multiple $\sigma_a$ values. Several distinct trends emerge from the simulations, reflecting how different gates respond to voltage miscalibration in a silicon spin qubit system.

**RX gate:** The $R_X(\pi/2)$ gate exhibits strong robustness against $\sigma_a$-type (multiplicative) errors. As shown in Fig. 3.1(a), the fidelity curves for different $\sigma_a$ values are closely clustered, indicating relatively weak sensitivity to proportional voltage scaling. This behavior arises from the linear dependence of the qubit's $g$-factor deviation ($\delta g$) on plunger gate voltage, $\delta g \approx kV$. A multiplicative error $a$ modifies this to $\delta g' = akV$, introducing a relative deviation of approximately $a - 1$. For the $\sigma_a$ range studied (0.001–0.009), this deviation is on the order of 0.1%–1%. While this can contribute to fidelity degradation, its effect is modest compared to additive errors, especially when $\sigma_b$ is non-negligible. In contrast, additive miscalibration $b$ shifts the detuning as $\delta g' = k(V + b)$, leading to a relative deviation of roughly $b/V$. Given that the typical control voltage $V$ is around 0.25 V, even small absolute offsets (e.g., $\sigma_b \sim 0.0001$) yield noticeable contributions to infidelity. As $\sigma_b$ increases, its impact dominates over $\sigma_a$, explaining the smooth fidelity degradation observed with $\sigma_b$. Overall, detuning miscalibration remains the primary error source for this gate, though subtle $\sigma_a$-dependent effects can still be found at low $\sigma_b$.

**Hadamard gate:** Figure 3.1(b) reveals a noise response qualitatively similar to that of the $R_X(\pi/2)$ gate. Like $R_X$, the Hadamard gate is predominantly detuning-driven and therefore exhibits strong resilience to $\sigma_a$. However, a slightly stronger dependence on $\sigma_a$ appears at low $\sigma_b$, which can be attributed to the larger rotation angle of $\pi$ in the Hadamard gate compared to $\pi/2$ in $R_X$. Nevertheless, across the parameter ranges explored, additive offset noise remains the dominant contributor to infidelity, and the Hadamard gate follows a similar overall trend to $R_X$. As $\sigma_b$ increases, the influence of $\sigma_a$ becomes negligible, with infidelity primarily determined by detuning offsets.

**Control-Z gate:** The CZ gate, shown in Fig. 3.1(c), exhibits a markedly different response due to its strong dependence on exchange coupling. Unlike detuning, the exchange interaction $J(V)$ depends exponentially on the applied voltage: $J(V) \propto \exp(\alpha V)$. A multiplicative error $a$ modifies this to $J'(V) \propto \exp(\alpha a V)$, amplifying even small $\sigma_a$ variations into substantial deviations in $J$. At small $\sigma_a$, fidelity degradation is already strongly driven by tunnel coupling fluctuations, while additive detuning offsets ($\sigma_b$) contribute a secondary effect. As $\sigma_a$ increases, the impact of $\sigma_b$ becomes comparatively negligible: the fidelity curves flatten and show little residual dependence on additive errors. This behavior highlights the CZ gate's acute sensitivity to exchange-mediated control errors, particularly in regions requiring precise tuning near an avoided crossing [54].

**$\sqrt{\text{SWAP}}$ gate:** The $\sqrt{\text{SWAP}}$ gate exhibits a noise response qualitatively similar to that of the CZ gate, reflecting their shared reliance on exchange-mediated entangling interactions. At small $\sigma_a$, fidelity degradation arises predominantly from multiplicative errors, with additive detuning offsets exerting a weaker influence. At large $\sigma_a$, the dominant role of tunnel coupling fluctuations causes the fidelity curves to become almost independent of $\sigma_b$, mirroring the behavior seen for CZ. This saturation effect underscores the exponential sensitivity of exchange interactions to voltage scaling, which can overwhelm detuning errors when $\sigma_a$ is large.

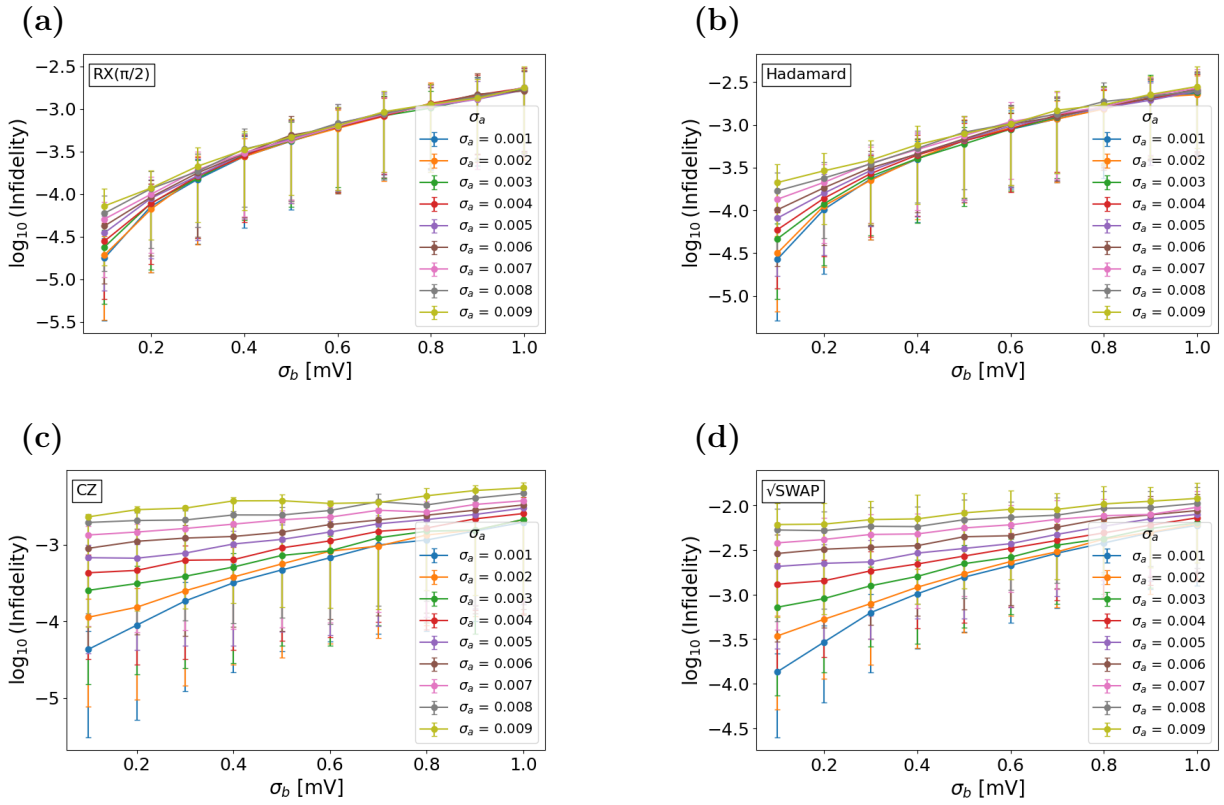



Figure 3.1: Simulated gate infidelity under voltage miscalibration. Each data point represents the average of 800 samples with Gaussian-distributed multiplicative ($a$) and additive ($b$) voltage noise. Error bars indicate the $20^{\text{th}}$–$80^{\text{th}}$ percentile range of the cumulative distribution of simulated fidelities, providing a measure of variability across noise realizations. **(a)** RX($\pi/2$) gate; **(b)** Hadamard gate; **(c)** CZ gate; **(d)** $\sqrt{\text{SWAP}}$ gate.

To validate our simulation results and gain deeper insight into error mechanisms, we

derive analytical expressions for the gate fidelities of $R_X(\pi/2)$ and $\sqrt{\text{SWAP}}$ under voltage miscalibration. These two gates serve as representative cases of detuning-driven and exchange-driven operations, respectively. Note that for simplicity, we consider constant pulses (square pulse shape) in the analytical treatment.

## Theoretical Fidelity: $R_X(\pi/2)$ Gate

The full Hamiltonian of the two-qubit system is given in Eq. (2.1). For the $R_X(\pi/2)$ gate, only the Zeeman detuning and resonant drive terms are relevant, as exchange coupling is not activated. Thus, the effective single-qubit Hamiltonian reduces to:

$$H(t) = \frac{\mu_B B_z}{2\hbar}\,\delta g(t)\,Z + \Omega_x(t)\,X + \Omega_y(t)\,Y, \tag{3.2}$$

where $\delta g(t) = g(\vec{V}(t), \vec{W}(t)) - g_0$ represents the deviation in the effective g-factor from its idle value.

### Step 1: Voltage Dependence of $\delta g$

The g-factor deviation $\delta g$ is approximated by a linear fit to the gate voltages in the vicinity of the operating point:

$$\delta g = c_1(V_1 - V_0) + c_2(V_2 - V_0) + c_3(W - W_0), \tag{3.3}$$

where $c_1, c_2, c_3$ are voltage-to-$\delta g$ conversion coefficients, and $V_0, W_0$ define the idle voltages.

Under miscalibration, each voltage is modified as:

$$V_i' - V_0 = a(V_i - V_0) + b, \quad (i = 1, 2), \tag{3.4}$$
$$W' - W_0 = a(W - W_0) + b. \tag{3.5}$$

This leads to a perturbed detuning:

$$\delta g' = c_1(V_1' - V_0) + c_2(V_2' - V_0) + c_3(W' - W_0), \tag{3.6}$$
$$= a \cdot \delta g + b(c_1 + c_2 + c_3). \tag{3.7}$$

**Step 2: Hamiltonian Before and After Miscalibration**

The ideal Hamiltonian over gate duration $T$ is:

$$H = \frac{\mu_B B_z}{\hbar}\,\delta g\, Z + \frac{\theta}{T}\left(\cos\phi\, X + \sin\phi\, Y\right). \tag{3.8}$$

After miscalibration, the Hamiltonian becomes:

$$H' = \frac{\mu_B B_z}{\hbar}\,\delta g'\, Z + \frac{\theta}{T}\left(\cos\phi\, X + \sin\phi\, Y\right), \tag{3.9}$$

$$= \frac{A'}{T} Z + \frac{\theta}{T}\left(\cos\phi\, X + \sin\phi\, Y\right), \tag{3.10}$$

where

$$A' = aA + T\frac{\mu_B B_z}{\hbar}\, b(c_1 + c_2 + c_3), \tag{3.11}$$

with $A = T\frac{\mu_B B_z}{\hbar}\delta g$.

We can rewrite both Hamiltonians in the standard form:

$$H = \frac{1}{2T}\theta\, n \cdot \sigma, \tag{3.12}$$

$$H' = \frac{1}{2T}\theta'\, n' \cdot \sigma. \tag{3.13}$$

**Step 3: RX($\pi/2$) Gate Specifics**

For the $R_X(\pi/2)$ gate, $\phi = 0$ (pure $X$ rotation) and ideally $A = 0$:

$$n = (1, 0, 0), \quad \theta = \frac{\pi}{2}.$$

The perturbed rotation axis is:

$$n' = \left(\frac{\theta}{\theta'},\, 0,\, \frac{A'}{\theta'}\right), \tag{3.14}$$

where

$$\theta' = \sqrt{A'^2 + \theta^2}. \tag{3.15}$$

**Step 4: Unitaries and Process Fidelity**

The ideal and perturbed unitaries are:

$$U_{\text{ideal}} = \cos\left(\frac{\theta}{2}\right) I - i \sin\left(\frac{\theta}{2}\right) n \cdot \sigma, \tag{3.16}$$

$$U_{\text{real}} = \cos\left(\frac{\theta'}{2}\right) I - i \sin\left(\frac{\theta'}{2}\right) n' \cdot \sigma. \tag{3.17}$$

The process fidelity is:

$$F_{\text{res}} = \cos\left(\frac{\theta}{2}\right) \cos\left(\frac{\theta'}{2}\right) + \sin\left(\frac{\theta}{2}\right) \sin\left(\frac{\theta'}{2}\right) \frac{\theta}{\theta'}. \tag{3.18}$$

**Step 5: Non-Resonant Qubit Contribution**

For the non-resonant qubit, ideally $\theta_n = 2\pi$ (identity up to phase). Miscalibration yields:

$$\theta'_n = \sqrt{\left(a\sqrt{4\pi^2 - \theta^2} + \Delta_z\right)^2 + \theta^2}, \tag{3.19}$$

where

$$\Delta_z = \frac{\mu_B B_z}{\hbar} bT(c_1 + c_2 + c_3).$$

The spectator qubit fidelity is:

$$F_{\text{nonres}} = \cos\left(\frac{\theta_n}{2}\right) \cos\left(\frac{\theta'_n}{2}\right) + \sin\left(\frac{\theta_n}{2}\right) \sin\left(\frac{\theta'_n}{2}\right) \frac{\theta_n}{\theta'_n}. \tag{3.20}$$

**Step 6: Total Two-Qubit Fidelity**

The overall fidelity is:

$$F_{2\text{q}} = -\frac{\sqrt{2}}{2} \cos\left(\frac{\theta'_n}{2}\right) \left[\cos\left(\frac{\theta'}{2}\right) + \sin\left(\frac{\theta'}{2}\right) \frac{\theta}{\theta'}\right]. \tag{3.21}$$

## Theoretical Fidelity: $\sqrt{\text{SWAP}}$ Gate

For the $\sqrt{\text{SWAP}}$ gate, exchange coupling $J$ plays the central role. The exchange interaction Hamiltonian is given by

$$H_{\text{ex}}(t) = J[\vec{V}(t), \vec{W}(t)] \, \frac{\vec{\sigma}_1 \cdot \vec{\sigma}_2}{4\hbar}. \tag{3.22}$$

The resulting unitary evolution contributes an interaction phase

$$\phi = \frac{TJ}{2\hbar}, \tag{3.23}$$

where $T$ is the gate duration.

The exchange coupling $J$ depends exponentially on the applied voltages:

$$J = C \, e^{\vec{\gamma}_1 \cdot (\vec{V}_1 - \vec{V}_0) + \vec{\gamma}_2 \cdot (\vec{V}_2 - \vec{V}_0) + \vec{\gamma}_3 \cdot (\vec{W} - \vec{W}_0)}. \tag{3.24}$$

When voltage miscalibration occurs, $J$ is perturbed to

$$J' = J^a \exp\left( b \sum_i \gamma_i \right). \tag{3.25}$$

This leads to a modified interaction phase:

$$\phi' = \frac{TJ'}{2\hbar} = \phi \, J^{a-1} \exp\left( b \sum_i \gamma_i \right). \tag{3.26}$$

The fidelity becomes

$$\begin{aligned} F = \Bigg| \exp\left[ \frac{i(\phi' - \phi)}{2} \right] & (\cos\phi \cos\phi' + \sin\phi \sin\phi' \\ & + \frac{i}{2} \left[ \sin\phi \cos\phi' - \cos\phi \sin\phi' \right] \Bigg) \Bigg|. \end{aligned} \tag{3.27}$$

Here, the global phase factor $\exp[i(\phi' - \phi)/2]$ vanishes upon taking the modulus, leaving

$$F = \left| \cos\phi \cos\phi' + \sin\phi \sin\phi' + \frac{i}{2} \left( \sin\phi \cos\phi' - \cos\phi \sin\phi' \right) \right|. \tag{3.28}$$

The real part dominates due to the suppression of the imaginary term by a factor of $1/2$. Neglecting higher-order contributions from the imaginary component, the fidelity simplifies to

$$F \approx \cos(\phi - \phi'). \tag{3.29}$$

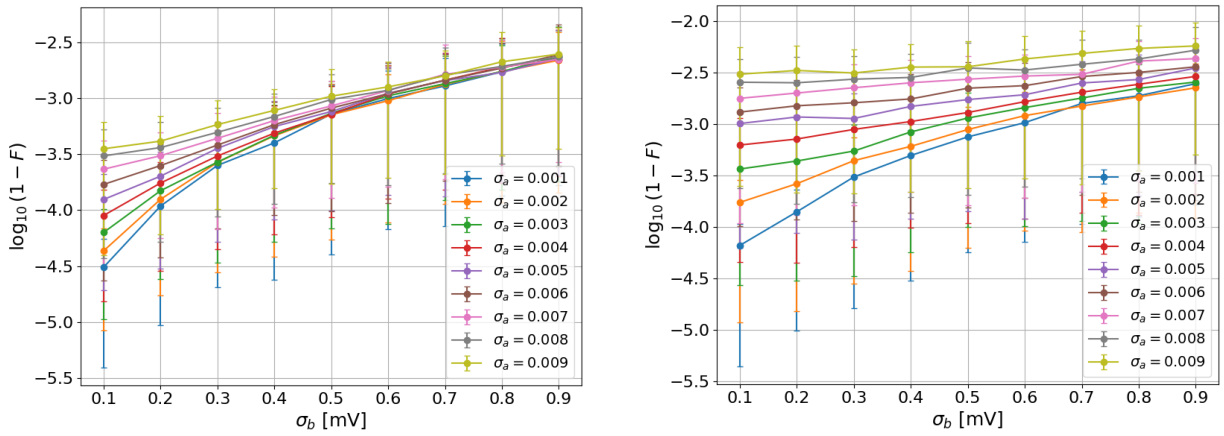
In our case, for a $\sqrt{\text{SWAP}}$ gate, the ideal interaction phase is $\phi = \pi/4$. This follows from Eq. (3.23) and the exchange coupling

$$J = \frac{\pi k \hbar}{T},$$

where $k$ denotes the SWAP exponent ($k = 1$ for a full SWAP). For $\sqrt{\text{SWAP}}$, $k = 1/2$, so substituting into Eq. (3.23) gives

$$\phi = \frac{T}{2\hbar} \cdot \frac{\pi k \hbar}{T} = \frac{\pi}{2} \cdot \frac{1}{2} = \frac{\pi}{4}.$$

This derivation highlights the exponential sensitivity of $\sqrt{\text{SWAP}}$ gates to both multiplicative and additive voltage errors, emphasizing the need for precise calibration in exchange-based operations.




(a) $RX(\pi/2)$ gate (b) $\sqrt{\text{SWAP}}$ gate

Figure 3.2: Analytically calculated fidelities of RX and $\sqrt{\text{SWAP}}$ gates as a function of $\sigma_b$ for several fixed $\sigma_a$ values.

**Comparison and Validation** The analytically calculated fidelities for the RX and $\sqrt{\text{SWAP}}$ gates are shown in Fig. 3.2. The theoretical predictions reproduce the overall trends observed in the simulation results of Fig. 3.1 with high consistency, confirming the validity of the derived expressions in capturing the dominant noise effects. However, slight deviations in the absolute fidelity values are noticeable, which may result from the simplified functional forms used in the fits ($\delta g(V)$ assumed linear and $J(V)$ assumed exponential), causing the extracted parameters to deviate slightly from their true values.

## 3.2 Random Telegraph Noise Effect on a Single Gate

Based on the RTN modeling framework introduced earlier, we now examine its quantitative impact on gate fidelity. For this, we superimpose RTN sequences onto the control voltages of representative single- and two-qubit operations. This section focuses on four gates: RX($\pi/2$), Hadamard, CZ, and $\sqrt{\text{SWAP}}$. Simulations were performed for various RTN switching times $\tau$ and amplitudes. Each data point represents an average over 200 noise realizations, and results are summarized in Fig. 3.3.

In Fig. 3.3, the vertical axis denotes the logarithmic infidelity $\log_{10}(1 - F)$, while the horizontal axis corresponds to the RTN amplitude in millivolts. Each colored curve represents a fixed $\tau$ ranging from $10^{-8}$ s to $10^{-4}$ s.

Across all four gates, the infidelity increases approximately quadratically with the noise amplitude, consistent with an empirical fit of the form

$$\log_{10}(1 - F) \propto \log_{10}(A^2),$$

or equivalently

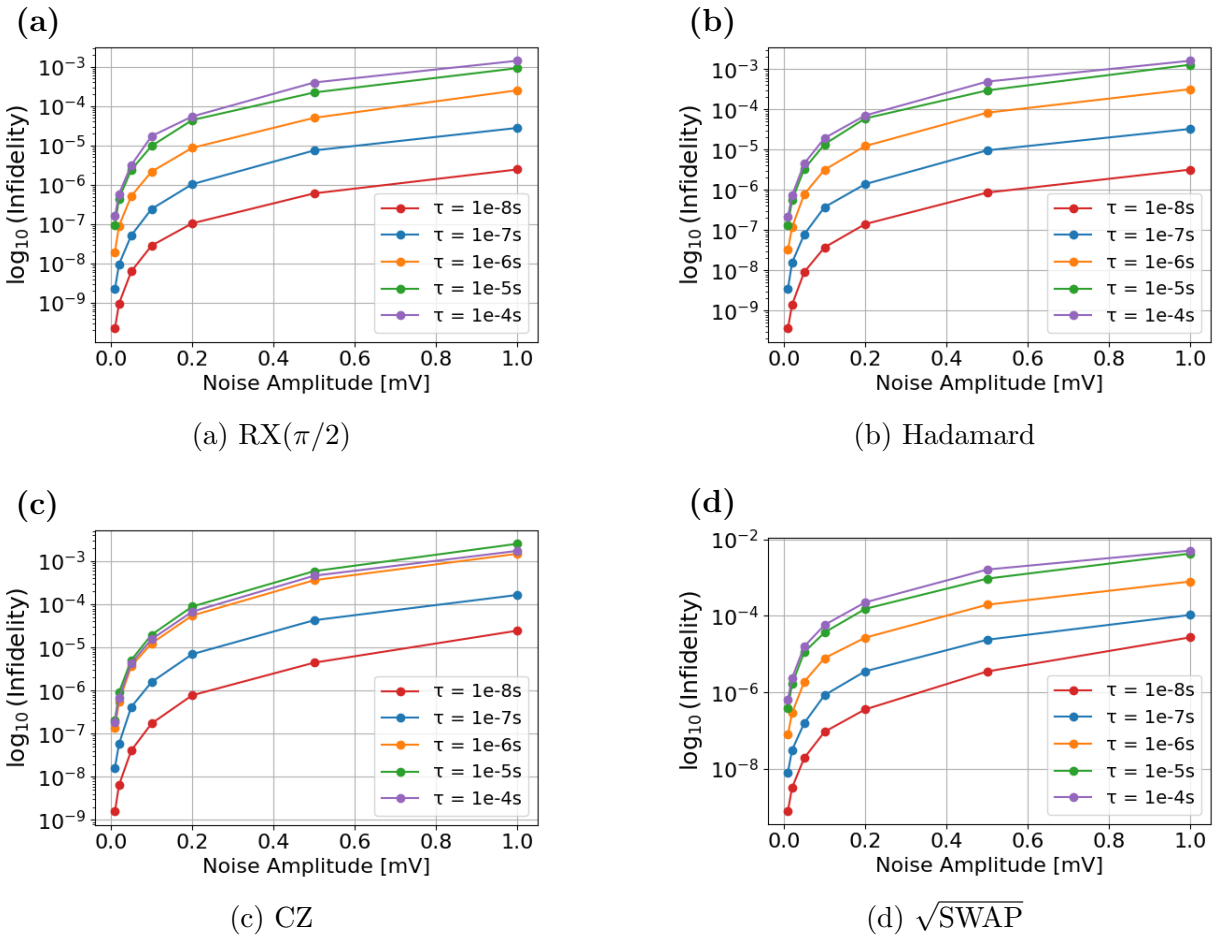
$$1 - F \approx aA^2,$$

where $a$ is a gate- and $\tau$-dependent proportionality constant. The fitted $a$ values for each gate and $\tau$ are summarized in Tables 3.1.

This quadratic dependence is physically consistent with the power spectral density (PSD) of a single RTN process (Eq. (2.2)). For slow noise ($\tau \gg t_g$, with $t_g$ the gate duration), the noise acts quasi-statically, leading to a linear scaling of variance with $\tau$ and quadratic scaling with $A$. Faster noise ($\tau \ll t_g$) averages out dynamically, leading to reduced infidelity.

Across gates, several key trends are evident:

- For RX and Hadamard, infidelity monotonically increases with $\tau$, saturating for $\tau = 10^{-5}$ s and $10^{-4}$ s where curves nearly overlap.
- For CZ, the largest $a$ occurs at $\tau = 10^{-5}$ s, slightly exceeding $\tau = 10^{-4}$ s, indicating mid-frequency noise dominates.
- For $\sqrt{\text{SWAP}}$, infidelity growth is the steepest, with $a$ an order of magnitude larger than RX/Hadamard, underscoring its heightened sensitivity to charge noise.




(a) RX($\pi/2$)

(b) Hadamard

(c) CZ

(d) $\sqrt{\text{SWAP}}$

Figure 3.3: Log-log plots of gate infidelity under RTN. Each curve corresponds to a fixed RTN switching time $\tau$ from $10^{-8}$ s to $10^{-4}$ s. The vertical axis shows $\log_{10}(1-F)$, and the horizontal axis shows RTN amplitude in millivolts.

Table 3.1: Quadratic fit coefficients $a$ for all gates at different $\tau$.

(a) RX($\pi/2$) gate

| $\tau$ (s) | $a$ |
|---|---|
| $1 \times 10^{-4}$ | $1.419 \times 10^{-3}$ |
| $1 \times 10^{-5}$ | $9.190 \times 10^{-4}$ |
| $1 \times 10^{-6}$ | $2.412 \times 10^{-4}$ |
| $1 \times 10^{-7}$ | $2.779 \times 10^{-5}$ |
| $1 \times 10^{-8}$ | $2.459 \times 10^{-6}$ |

(b) Hadamard gate

| $\tau$ (s) | $a$ |
|---|---|
| $1 \times 10^{-4}$ | $1.624 \times 10^{-3}$ |
| $1 \times 10^{-5}$ | $1.291 \times 10^{-3}$ |
| $1 \times 10^{-6}$ | $3.199 \times 10^{-4}$ |
| $1 \times 10^{-7}$ | $3.300 \times 10^{-5}$ |
| $1 \times 10^{-8}$ | $3.209 \times 10^{-6}$ |

(c) CZ gate

| $\tau$ (s) | $a$ |
|---|---|
| $1 \times 10^{-4}$ | $1.740 \times 10^{-3}$ |
| $1 \times 10^{-5}$ | $2.541 \times 10^{-3}$ |
| $1 \times 10^{-6}$ | $1.491 \times 10^{-3}$ |
| $1 \times 10^{-7}$ | $1.653 \times 10^{-4}$ |
| $1 \times 10^{-8}$ | $2.448 \times 10^{-5}$ |

(d) $\sqrt{\text{SWAP}}$ gate

| $\tau$ (s) | $a$ |
|---|---|
| $1 \times 10^{-4}$ | $5.096 \times 10^{-3}$ |
| $1 \times 10^{-5}$ | $4.227 \times 10^{-3}$ |
| $1 \times 10^{-6}$ | $7.889 \times 10^{-4}$ |
| $1 \times 10^{-7}$ | $1.055 \times 10^{-4}$ |
| $1 \times 10^{-8}$ | $2.735 \times 10^{-5}$ |

Among the four gates studied, the two-qubit RTN and $\sqrt{\text{SWAP}}$ gates exhibit notably larger $a$ coefficients compared to single-qubit operations. This heightened sensitivity can be attributed to the nonlinear dependence of the exchange interaction on the control voltages. Charge fluctuations directly perturb the exchange coupling $J$, leading to amplified errors in gates whose Hamiltonians rely critically on this parameter. In contrast, single-qubit gates, such as RX and Hadamard, predominantly depend on local $g$ factor tuning, which is less susceptible to charge noise.

Furthermore, for the long switching time considered ($\tau = 10^{-5} - 10^{-4}$ s), the RTN approaches the quasi-static regime. In this limit, the noise effectively acts as a slowly varying offset in the gate voltages during each operation. This situation mimics a miscalibration error, where each noise realization shifts the system slightly off the intended operating point.

It is also noteworthy that with increasing $\tau$, the system enters a progressively more static noise regime, where each RTN trace effectively acts as a constant offset to the voltage pulse. As a result, for a fixed average noise amplitude, noise traces with $\tau$ longer than or comparable to the gate duration have an equivalent impact on the fidelity of any quantum gate. This behavior is clearly illustrated in Fig. 3.1, where the fidelity curves for

$\tau = 10\,\mu$s and $\tau = 100\,\mu$s almost overlap across all gates. This convergence reflects the transition from dynamically fluctuating noise to quasi-static offset errors as $\tau$ increases.

## 3.3 Error Analysis via Quantum Process Tomography

### Error Characterization via Kraus Operator Decomposition

To gain detailed insights into noise-induced errors for representative quantum gates, we perform QPT simulations on three gates: RX($\pi/2$), Hadamard, and CZ. From the process matrix $\chi$, the set of Kraus operators $\{K_i\}$ describing the noisy channel are extracted using the relation:

$$\mathcal{E}(\rho) = \sum_i K_i \rho K_i^\dagger$$

where each $K_i$ encapsulates a distinct error process.

To focus exclusively on noise effects and separate them from the ideal gate action, we apply a transformation that removes the ideal unitary $U_{\text{gate}}$ from each Kraus operator:

$$K_i' = U_{\text{gate}}^\dagger K_i$$

This isolates residual errors relative to the intended operation, enabling a clearer identification of error types.

**Kraus Operator Norm Analysis.** We quantify each $K_i'$ by its Frobenius norm:

$$\|K_i'\|_F = \frac{1}{\sqrt{2^n}} \sqrt{\text{Tr}(K_i'^\dagger K_i')}$$

normalized by $\sqrt{2^n}$ (where $n$ is the number of qubits) so that an ideal channel produces $\|K_N\|_F = 1$ for the dominant Kraus operator $K_N$and all other $\|K_i\|_F = 0$. Figures 3.4a–3.4c show $\|K_i'\|$ versus noise amplitude for all six Kraus operators in each gate, with $1 - \|K_6'\|$ plotted for clarity since $K_6$ dominates in the noise-free limit.

Across all gates, a consistent hierarchy $\|K_6\| > \|K_5\| > \cdots > \|K_1\|$ is observed, and the norms increase almost monotonically with the voltage noise amplitude. This reflects the progressive leakage of fidelity from $K_6$ to subdominant error processes.

**Error Type Decomposition.** Each $K_i'$ is decomposed into the Pauli operators:

$$K_i' = \sum_j c_{ij} P_j,$$

where $c_{ij}$ are complex coefficients that indicate the contribution of each Pauli basis element $P_j$. Figures 3.5–3.7 show the dominant Pauli coefficients ($|c_{ij}| > 0.005$ for CZ, $> 0.001$ for RX and Hadamard) as functions of noise amplitude. For $K_6$, which reflects fidelity loss, we observe a quadratic dependence on voltage noise and fit it accordingly.

Empirically, we find that each $K_i'$, $i = 1, \ldots, 5$, scales approximately linearly with the noise amplitude:

$$K_i'(V) \approx a_i V \left(b_{i1} P_1 + b_{i2} P_2 + \ldots\right),$$

where $a_i$ is the slope obtained from fitting the Kraus norm $\|K_i'\|$, and $b_{ij}$ are normalized Pauli weights satisfying $\sum_j b_{ij}^2 = 1$. In our fitting procedure, however, we first extract a common factor $c_i$ from the dominant Pauli coefficients and write

$$K_i'(V) = c_i V (s_{i1} P_1 + s_{i2} P_2 + \ldots),$$

where $s_{ij}$ are the unnormalized Pauli slopes. To match the theoretical form, we define a normalization factor $\sqrt{\sum_j s_{ij}^2}$ and rewrite

$$K_i'(V) \approx \underbrace{c_i \sqrt{\sum_j s_{ij}^2}}_{\text{Norm Scale}} V \left(b_{i1} P_1 + b_{i2} P_2 + \ldots\right),$$

where $b_{ij} = s_{ij} / \sqrt{\sum_j s_{ij}^2}$. Here, we define the *Norm Scale* as the proportionality factor between the Kraus operator norm and the noise amplitude; it quantifies how the overall magnitude of $K_i'$ scales with increasing noise strength. We verified that this Norm Scale closely matches the independently obtained $a_i$ from the Kraus norm fit, with only minor deviations attributable to fitting differences. In Tables 3.5–3.7, the first column lists the Norm Scale, representing the effective strength of each Kraus operator, and the second column shows the corresponding normalized dominant Pauli error terms.

**CZ Gate.** For the CZ gate (Fig. 3.5), dominant error terms include $ZZ$, $IZ$, $ZI$, $XX$, and $YY$. This is consistent with the structure of the underlying Hamiltonian, which contains contributions from $IZ$, $ZI$, and $(XX + YY + ZZ)$ terms:

$$H_{\text{CZ}} = \delta g_1 \, \sigma_z^1 + \delta g_2 \, \sigma_z^2 + J(t) \, (\sigma_x^1 \sigma_x^2 + \sigma_y^1 \sigma_y^2 + \sigma_z^1 \sigma_z^2).$$

Since the coefficients of $IZ$ and $ZI$ terms are of comparable magnitude—reflecting similar qubit frequencies—the system cannot be approximated by a pure Ising interaction. Instead, the observed dominant error channels correspond to linear combinations of these native Hamiltonian terms, with $ZZ$, $IZ$, $ZI$, $XX$, and $YY$ naturally arising from direct noise coupling to these components.

**RX($\pi/2$) Gate.** The RX gate (Fig. 3.6) shows dominant $IZ$ and $ZI$ errors, consistent with phase noise and crosstalk between qubits during single-qubit control. The appearance of $IY$ and $IX$ terms reflects rotation-axis misalignments due to RTN-induced fluctuations in the drive amplitude and phase. Notably, $XX$, $YY$ and $ZZ$-type errors are absent, as expected for a single-qubit operation.

**Hadamard Gate.** For the Hadamard gate (Fig. 3.7), dominant error types are again $IZ$, $ZI$, and $IX$. This pattern is consistent with phase noise sensitivity during a rotation around an axis in the $x$-$z$ plane. The presence of $IY$ and $XI$ further indicates susceptibility to drive imperfections and cross-qubit coupling.

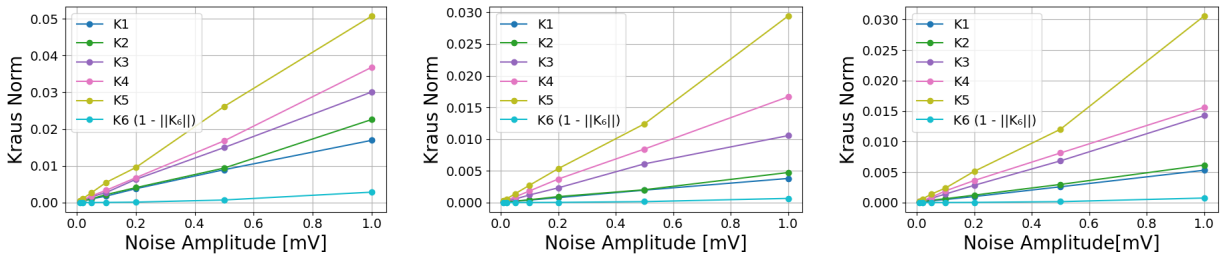
This Kraus operator analysis provides a detailed picture of error channels in silicon spin qubit gates. By isolating noise-induced errors and decomposing them into Pauli terms, we reveal gate-specific noise sensitivities: Ising-type errors in CZ and phase/crosstalk errors in RX and Hadamard. These insights can inform the design of noise-adaptive control pulses, error mitigation strategies, and robust quantum gate protocols tailored to dominant noise mechanisms in semiconductor platforms.

### Coherent Error Extraction and Correction

We next implement the unitary error correction method described in Section 2.3.2 to examine its impact on gate fidelities under RTN. This method isolates the dominant coherent error component from the process matrix by identifying the leading Kraus operator $K_{\text{dom}}$, projecting out the ideal gate, and computing an effective unitary correction $U_{\text{err}}$. Applying $U_{\text{err}}^{\dagger}$ to the noisy final state yields a corrected output, effectively mitigating the coherent portion of the noise.

When RTN is applied to the control voltages, two broad error categories emerge:

- **Coherent (unitary) errors:** These originate from the voltage dependence of the Hamiltonian parameters, such as $\delta g(V(t))$ and $J(V(t))$. Noise in $V(t)$ perturbs these




(a) CZ gate (b) RX($\pi/2$) gate (c) Hadamard gate

Figure 3.4: Kraus operator norms versus noise amplitude for three representative gates: CZ, RX($\pi/2$), and Hadamard. Each panel shows the six dominant Kraus operators ($K_1$–$K_6$), where $K_6$ corresponds to the operator with the largest norm. For $K_6$, we plot $1 - \|K_6\|$. The norms are computed after undoing the respective ideal unitary from each Kraus operator.

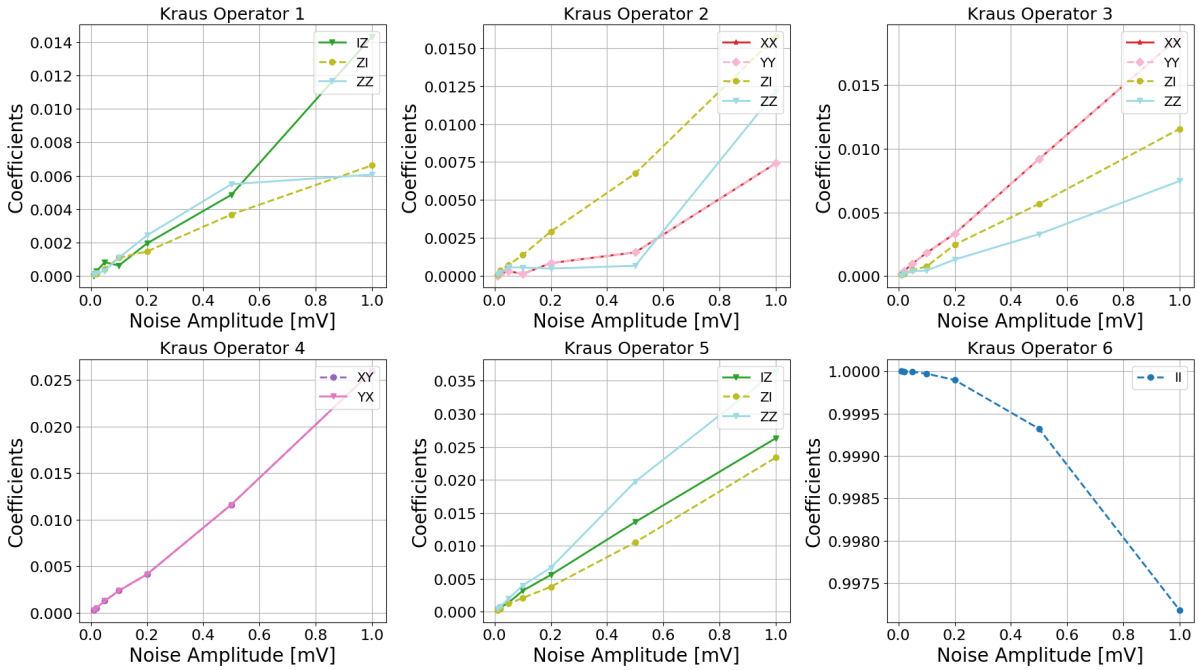
quantities, thereby distorting the corresponding Hamiltonian terms. For exchange gates, this effect is particularly strong because $J(V)$ depends exponentially on voltage, so even small fluctuations induce significant systematic errors. In contrast, for single-qubit gates, $\delta g(V)$ depends linearly on $V$; fluctuations tend to average out, leaving only weak coherent deviations.

- **Incoherent errors:** These arise from ensemble-averaging the resulting quantum channels obtained from many RTN realizations with the same $\tau$ and amplitude. If the noisy evolution is similar across realizations (as in the case of fast RTN), little averaging-induced decoherence is introduced. Conversely, if different realizations lead to very different gate actions (as in slow RTN), the ensemble average produces an effectively non-unitary error channel dominated by dephasing-like effects.

Figure 3.8 illustrates these effects for the CZ gate. In both panels, larger noise amplitudes always reduce fidelity, and the fraction of coherent error increases with amplitude. Comparing different correlation times, a larger $\tau$ leads to lower overall fidelity but a higher incoherent fraction that cannot be corrected by a unitary operation. In contrast, for smaller $\tau$, the average fidelity is higher, but the errors are dominated by coherent contributions, making unitary correction more effective.

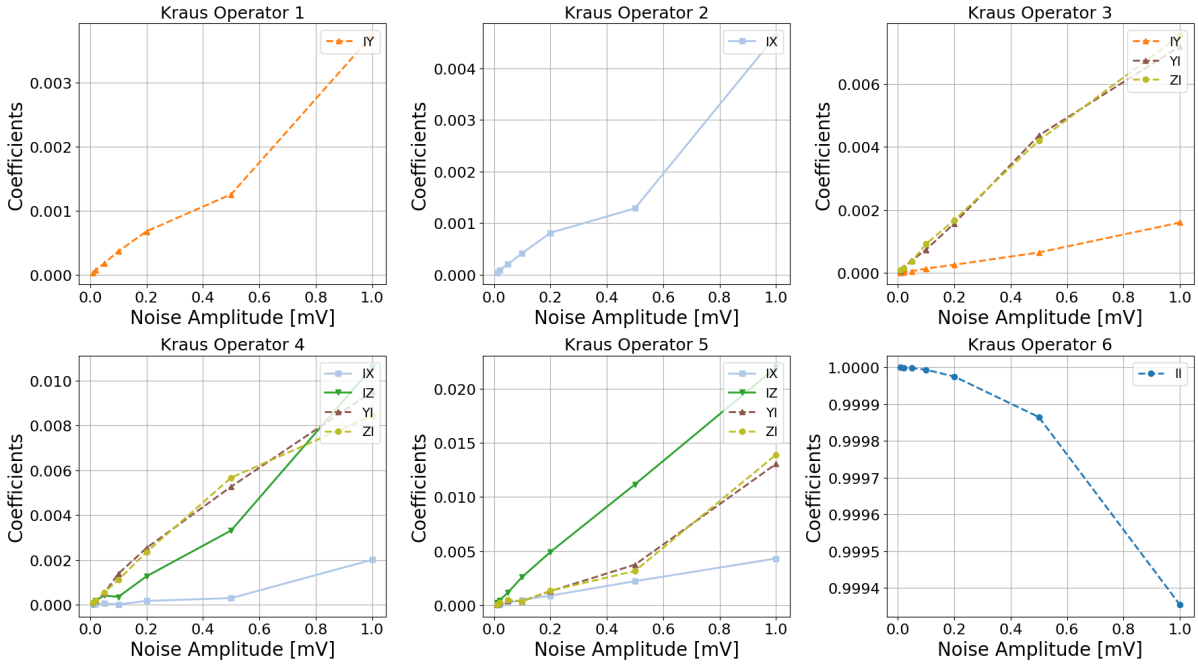
To quantify the effectiveness of this approach, We define the relative *infidelity* improvement as

$$\text{Improvement} = \left| \frac{I_{\text{after}} - I_{\text{before}}}{I_{\text{before}}} \right| \times 100\%, \qquad I = 1 - F. \tag{3.30}$$



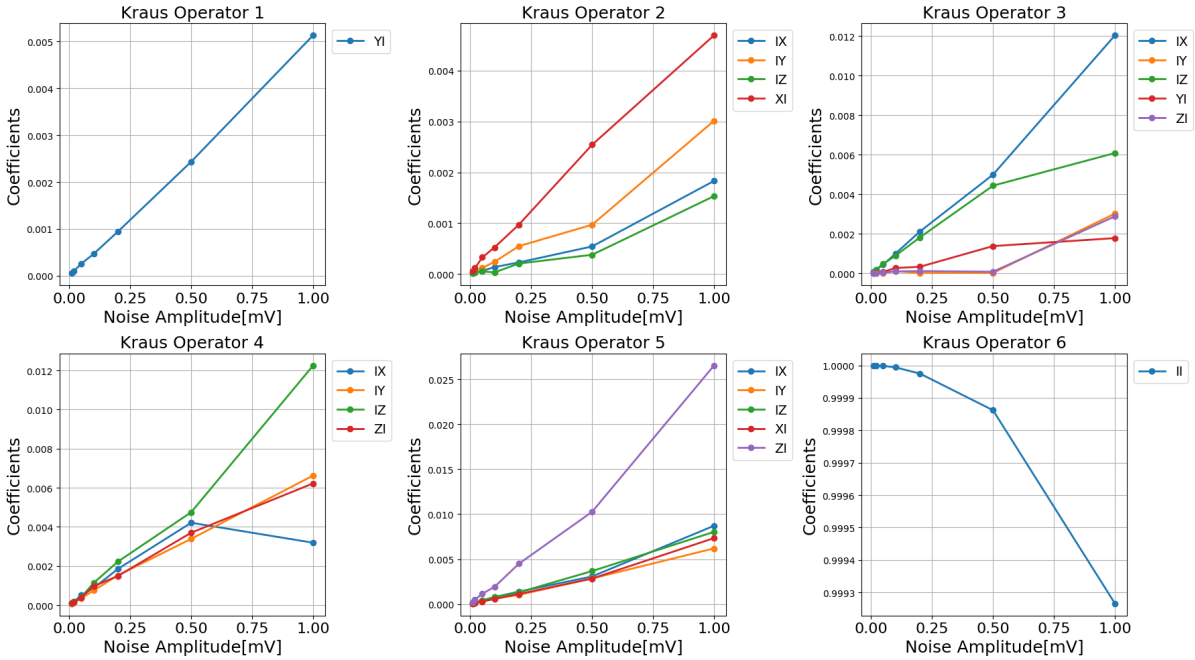

| **Norm scale** $[V^{-1}]$ | **Error Type** |
|---|---|
| K1: 16.7 | $0.832IZ + 0.393ZI + 0.392ZZ$ |
| K2: 21.4 | $0.328XX + 0.328YY + 0.725ZI + 0.510ZZ$ |
| K3: 29.9 | $0.627XX + 0.627YY + 0.389ZI + 0.248ZZ$ |
| K4: 36.3 | $0.707XY + 0.707YX$ |
| K5: 50.8 | $0.516IZ + 0.456ZI + 0.725ZZ$ |

Figure 3.5: Pauli decomposition of the six Kraus operators for the CZ gate under voltage noise. The top panel shows dominant Pauli coefficients for each Kraus operator as a function of noise amplitude, displaying only terms exceeding a threshold of 0.005 at maximum amplitude. The bottom table summarizes linear fits for the first five Kraus operators. The first column lists the Norm scale (effective strength) of each Kraus operator, and the second column shows the normalized dominant Pauli error terms. Coefficients are computed after undoing the gate unitary transformation (applying $U_{\text{gate}}^{\dagger}$).




| **Norm Scale** $[V^{-1}]$ | **Error Type** |
|---|---|
| K1: 3.57 | $1IY$ |
| K2: 4.37 | $1IX$ |
| K3: 10.7 | $0.147IY + 0.688YI + 0.710ZI$ |
| K4: 16.6 | $0.114IX + 0.621IZ + 0.572YI + 0.524ZI$ |
| K5: 28.8 | $0.150IX + 0.758IZ + 0.439YI + 0.459ZI$ |

Figure 3.6: Pauli decomposition of the six Kraus operators for the RX gate under voltage noise. The top panel shows dominant Pauli coefficients for each Kraus operator as a function of noise amplitude, displaying only terms exceeding a threshold of 0.001 at maximum amplitude. The bottom table summarizes linear fits for the first five Kraus operators. The first column lists the Norm scale (effective strength) of each Kraus operator (the product of the common fit factor and a normalization factor), and the second column shows the normalized dominant Pauli error terms. Coefficients are computed after undoing the gate unitary transformation (applying $U_{\text{gate}}^{\dagger}$).




| **Norm Scale** $[V^{-1}]$ | **Error Type** |
|---|---|
| K1: 5.11 | $1YI$ |
| K2: 6.00 | $0.295IX + 0.483IY + 0.245IZ + 0.787XI$ |
| K3: 14.2 | $0.842IX + 0.195IY + 0.447IZ + 0.136YI + 0.185ZI$ |
| K4: 15.5 | $0.231IX + 0.427IY + 0.775IZ + 0.405ZI$ |
| K5: 29.9 | $0.281IX + 0.205IY + 0.265IZ + 0.240XI + 0.867ZI$ |

Figure 3.7: Pauli decomposition of the six dominant Kraus operators for the Hadamard gate under voltage noise. The top panel shows the dominant Pauli coefficients (threshold = 0.001) as a function of noise amplitude, for the six Kraus operators with the largest norms. The bottom table summarizes linear fits for the first five Kraus operators. The first column lists the Norm scale (effective strength) of each Kraus operator, and the second column shows the normalized dominant Pauli error terms. Coefficients are computed after undoing the Hadamard unitary transformation.

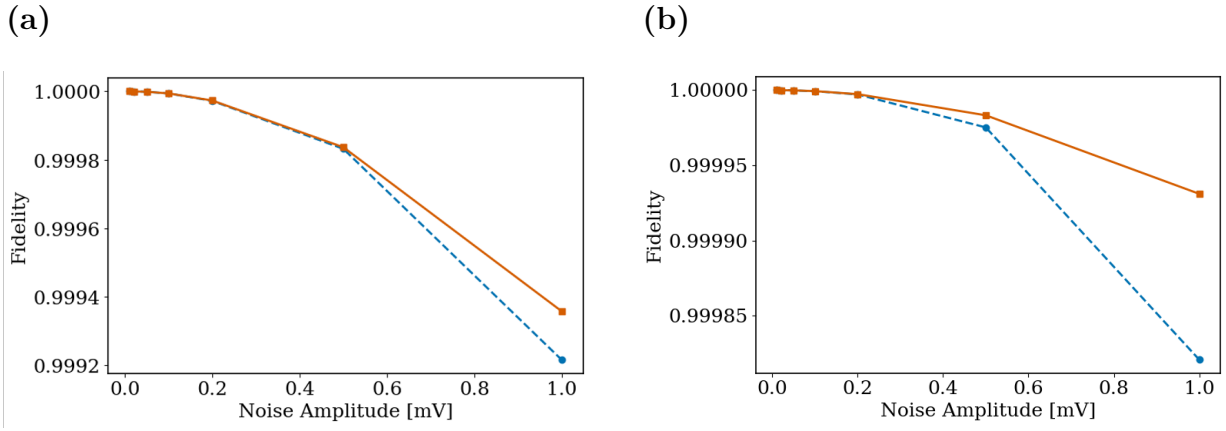



Figure 3.8: CZ gate fidelity vs. RTN amplitude. (a): $\tau = 10^{-7}$ s. (b): $\tau = 10^{-8}$ s. Blue: before correction; orange: after correction.

Here $I_{\text{before}}$ and $I_{\text{after}}$ denote the infidelities before and after correction, respectively. This form emphasizes that the numerator represents the change in infidelity due to correction, while the denominator normalizes by the original infidelity. Table 3.2 reports the relative infidelity improvements for the CZ gate at a fixed noise amplitude of 1 mV across different switching times.

Table 3.2: Relative infidelity improvement for the CZ gate at $A = 1$ mV.

| $\tau$ (s) | Improvement (%) |
|---|---|
| $1 \times 10^{-5}$ | 0.67 |
| $1 \times 10^{-6}$ | 1.30 |
| $1 \times 10^{-7}$ | 18.08 |
| $1 \times 10^{-8}$ | 61.54 |

The strong improvement at small $\tau$ can be traced to the nonlinear voltage dependence of the exchange interaction $J$. Since $J(V) \propto e^{\alpha V}$, random fluctuations in $V(t)$ lead to large systematic distortions in the accumulated entangling phase, which appear as coherent errors that are consistently captured by the dominant Kraus operator and can be corrected. As $\tau$ decreases, high-frequency fluctuations vary little between individual runs, so averaging over many repetitions does not introduce significant incoherent errors, leaving a larger coherent component that can be corrected by a unitary operation. In contrast, slow RTN acts like quasistatic voltage offsets: Each realization shifts the operation differently, and averaging over many runs produces predominantly incoherent errors that cannot be

corrected by a unitary operation.

For single-qubit gates such as RX($\pi/2$) and the Hadamard gate, the fidelity improvement achievable through unitary correction is negligible. Their approximately linear response to $V(t)$ causes fluctuations in $\delta g$ to largely cancel over the course of the gate, resulting in minimal coherent distortion. Consequently, the errors are predominantly stochastic, and unitary correction provides little benefit.

These findings highlight that the effectiveness of coherent error correction depends critically on both the nonlinearity of the system's voltage-to-Hamiltonian mapping and the relation between the RTN correlation time and the gate duration.

# Chapter 4

# Noise Analysis in Variational Quantum Eigensolvers

## 4.1 Variational Quantum Eigensolvers

The Variational Quantum Eigensolver (VQE) algorithm has been extensively discussed in the literature [55, 56, 57]. Here, we provide a concise summary of its workflow, as illustrated in Fig. 4.1. A typical VQE process consists of the following steps:

1. Reformulate the given Hamiltonian.
2. Initialize the system in the Hartree-Fock ground state.
3. Construct a trial state by selecting an ansatz with adjustable parameters and setting their initial values:
$$|\phi(\theta)\rangle = U(\theta)|\phi_0\rangle$$
4. Measure the energy expectation value of the trial state $|\phi(\theta)\rangle$ with a quantum computer.
$$C(\theta) = \langle\phi(\theta)|H|\phi(\theta)\rangle$$
5. Check convergence and use a classical optimizer, such as the Nelder–Mead simplex method, to update the parameters and iteratively lower the energy.
6. Repeat this process until convergence is achieved.

The ultimate goal of VQE is to determine the parameterization of $|\phi\rangle$ that minimizes the expectation value of the Hamiltonian. Mathematically, this corresponds to approximating

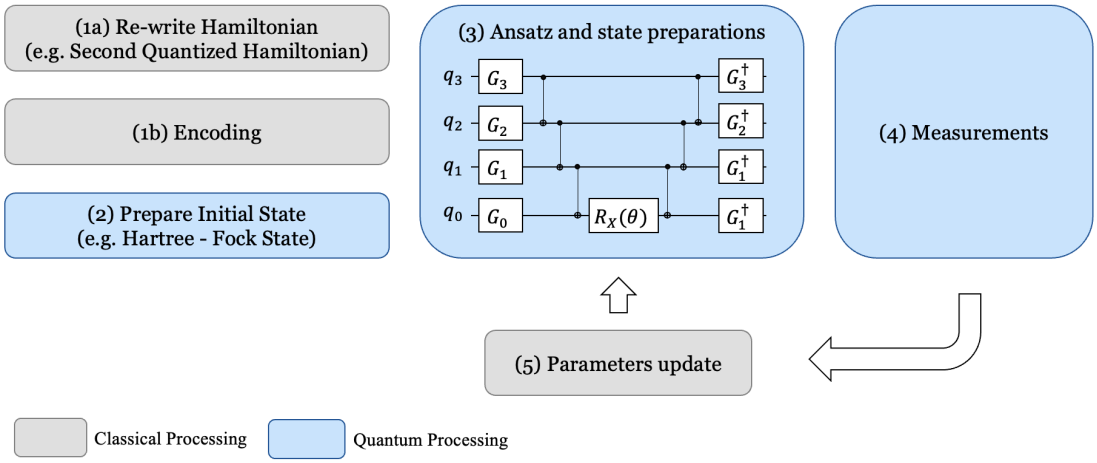



Figure 4.1: VQE Pipeline (1) Preparation steps: (a) Express the given Hamiltonian as a quantum observable wavefunction; (b) Encode from fermionic space to Pauli space; (2) Find initial state: Usually use Hartree-Fock method; (3) Ansatz Selection: Prepare trial state with selected ansatz; (4) Measurements; (5) Parameter Update: Optimize the parameter on the classical computer.

the eigenvector of the Hermitian operator $H$ associated with the lowest eigenvalue $E_0$.

$$E_0 \leq \frac{\langle\phi|H|\phi\rangle}{\langle\phi|\phi\rangle}$$

The VQE begins with the molecular Hamiltonian, which describes the total energy of a molecule consisting of $K$ nuclei and $N$ electrons. The general form of the Hamiltonian is given by [3]:

$$\begin{aligned} H = &- \sum_i \left( \frac{\hbar^2}{2m_e} \nabla_i^2 \right) - \sum_I \left( \frac{\hbar^2}{2M_I} \nabla_I^2 \right) \\ &- \sum_{i,I} \left( \frac{e^2}{4\pi\epsilon_0} \frac{Z_I}{|\vec{r}_i - \vec{R}_I|} \right) + \frac{1}{2} \sum_{i \neq j} \left( \frac{e^2}{4\pi\epsilon_0} \frac{1}{|\vec{r}_i - \vec{r}_j|} \right) \\ &+ \frac{1}{2} \sum_{I \neq J} \left( \frac{e^2}{4\pi\epsilon_0} \frac{Z_I Z_J}{|\vec{R}_I - \vec{R}_J|} \right) \end{aligned} \tag{4.1}$$

where the $I$th nucleus is characterized by $M_I$, $\vec{R}_I$, and $Z_I$, which denote its mass, position, and atomic number, respectively. The position of the $i$th electron is given by $\vec{r}_i$. The first two terms in the Hamiltonian represent the kinetic energy of the electrons and nuclei. The last three terms describe the Coulomb interactions: electron-nucleus attraction, electron-electron repulsion, and nucleus-nucleus repulsion.

To simplify the problem, we apply the Born-Oppenheimer approximation [58], which treats the nuclei as classical point charges and assumes that electronic motion is decoupled from nuclear motion. Under this approximation, the molecular Hamiltonian reduces to the electronic Hamiltonian and is given by:

$$H = T_e + V_{ne} + V_{ee}, \tag{4.2}$$

where $T_e$ represents the kinetic energy of the electrons, $V_{ne}$ describes the electron-nucleus interactions, and $V_{ee}$ accounts for the electron-electron repulsion.

However, the Hamiltonian is still too complex to solve directly in terms of electron positions and spins, VQE then represents the molecular system using wavefunctions. Constructing an accurate electronic wavefunction requires choosing an appropriate basis set. Most VQE studies employ minimal-sized Slater-type orbitals (STO). Once the single-particle basis functions are selected, many-body basis functions for the electronic wavefunction can be built by taking their products, forming the foundation for subsequent quantum simulations.

To facilitate the mapping of electronic structure problems onto quantum computers, we employ the formalism of second quantization. This approach expresses the molecular Hamiltonian in terms of fermionic creation and annihilation operators, which encode the occupation of quantum states in a more structured manner.

Therefore, for a given hydrogen molecule, the second quantized form of the fermionic Hamiltonian is given by:

$$H = \sum_{p,q} h_{pq} a_p^\dagger a_q + \frac{1}{2} \sum_{p,q,r,s} h_{pqrs} a_p^\dagger a_q^\dagger a_r a_s, \tag{4.3}$$

where the matrix elements $h_{pq}$ and $h_{pqrs}$ are defined as:

$$h_{pq} = \int dx\, \phi_p^*(x) \left( -\frac{\nabla^2}{2} - \sum_I \frac{Z_I}{|r - R_I|} \right) \phi_q(x) \tag{4.4}$$

$$h_{pqrs} = \int dx_1\, dx_2\, \frac{\phi_p^*(x_1)\phi_q^*(x_2)\phi_r(x_2)\phi_s(x_1)}{|r_1 - r_2|}. \tag{4.5}$$

This fermionic system can be mapped to a qubit-based representation using the Jordan-Wigner transformation [59]. This transformation encodes the fermionic Hamiltonian in terms of Pauli operators $P_k$, enabling efficient simulation on a quantum computer. Through this mapping, the Hamiltonian takes the form:

$$H = \sum_k h_k P_k, \tag{4.6}$$

where $h_k$ are real coefficients. Consequently, the variational principle can be reformulated as

$$E_0 \leq \min_\theta \left( \sum_k h_k \langle \phi(\theta) | P_k | \phi(\theta) \rangle \right). \tag{4.7}$$

This formulation allows for iterative optimization of $\theta$ to approximate the ground-state energy of the system. To perform this optimization, various ansatzes are employed for preparing the trial state. One of the most effective ansatzes in quantum chemistry is the Unitary Coupled Cluster (UCC) ansatz, which is a variation of the classical Coupled Cluster (CC) method that ensures unitarity.

The CC method is a post-Hartree-Fock approach that employs an exponential parameterization of electron correlation effects, capturing many-body interactions beyond the mean-field approximation. The total energy in the CC framework is given by:

$$E = E_{\text{HF}} + E_{\text{corr}}, \tag{4.8}$$

where $E_{\text{HF}}$ is the Hartree-Fock energy and $E_{\text{corr}}$ represents the correlation energy. The Coupled Cluster wavefunction is expressed as:

$$|CC\rangle = e^T |HF\rangle, \tag{4.9}$$

where $T$ is the cluster operator. However, since $e^T$ is not unitary—due to the presence of non-Hermitian components in $T$—it cannot be directly implemented on a quantum computer. A key advantage of the UCC ansatz over conventional CC methods is its unitary

structure, which ensures numerical stability and compatibility with quantum computation. The UCC ansatz is defined as:

$$|\psi\rangle = e^{T-T^\dagger}|\psi_0\rangle, \tag{4.10}$$

where the cluster operator is given by:

$$\hat{T}_1 = \sum_{i\in\text{virt},\,\alpha\in\text{occ}} t_{i\alpha} a_i^\dagger a_\alpha, \tag{4.11}$$

$$\hat{T}_2 = \sum_{i,j\in\text{virt},\,\alpha,\beta\in\text{occ}} t_{ij\alpha\beta} a_i^\dagger a_j^\dagger a_\alpha a_\beta. \tag{4.12}$$

Here, "virt" refers to unoccupied orbitals above the Fermi level, and "occ" denotes the orbitals that are fully occupied in the reference Hartree–Fock determinant. By incorporating the UCC ansatz within the VQE framework, quantum computers can approximate the ground-state energies of molecular systems with improved accuracy, making this method a promising approach for quantum chemistry applications.

### 4.1.1 Variational Quantum Eigensolvers Simulation - Hydrogen Molecule

The hydrogen molecule ($H_2$) is the simplest neutral molecule, consisting of two hydrogen atoms. Our goal is to accurately compute its ground-state energy as a function of the internuclear distance $R$. This is achieved using the VQE framework as described in the previous section. For simulations of the $H_2$ molecule within the minimal STO-3G basis, we construct a 4-qubit Hamiltonian by mapping its fermionic representation to a qubit-based form via the Jordan-Wigner transformation:

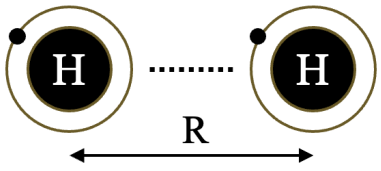



Figure 4.2: Hydrogen molecule with nuclei separated by distance R

$$
\begin{aligned}
H = & h_0 I + h_1 Z_0 + h_2 Z_1 + h_3 Z_2 + h_4 Z_3 + h_5 Z_0 Z_1 + h_6 Z_0 Z_2 \\
& + h_7 Z_1 Z_2 + h_8 Z_0 Z_3 + h_9 Z_1 Z_3 + h_{10} Z_2 Z_3 \\
& + h_{11} Y_0 Y_1 X_2 X_3 + h_{12} X_0 Y_1 Y_2 X_3 \\
& + h_{13} Y_0 X_1 X_2 Y_3 + h_{14} X_0 X_1 Y_2 Y_3
\end{aligned} \tag{4.13}
$$

where the coefficients $h_i$ depend on the internuclear distance $R$ and are obtained from calculations of electronic structures. In our study, these values were computed using the open-source quantum chemistry package Psi4 [60]. The numerical values of these coefficients are provided in Appendix A.

The reference state for our ansatz is chosen as:

$$|\psi_0\rangle = |0011\rangle$$

which corresponds to the Hartree-Fock configuration.

The unitary coupled-cluster (UCC) ansatz operator for $H_2$ in the STO-3G basis is given by:

$$U = \exp\left[\theta\left(a_2^\dagger a_3^\dagger a_1 a_0 - a_0^\dagger a_1^\dagger a_3 a_2\right)\right] \tag{4.14}$$

where $\theta$ represents the cluster amplitude. Applying the Jordan-Wigner transformation, the UCC operator transforms into:

$$U = \exp\left(\theta \frac{i}{8}\begin{pmatrix} X_3Y_2X_1X_0 + Y_3X_2X_1X_0 \\ +Y_3Y_2Y_1X_0 + Y_3Y_2X_1Y_0 \\ -X_3X_2Y_1X_0 - X_3X_2X_1Y_0 \\ -Y_3X_2Y_1Y_0 - X_3Y_2Y_1Y_0 \end{pmatrix}\right) \tag{4.15}$$

Since all Pauli terms originate from the same excitation operators and mutually commute, the exponentials can be decomposed into individual Pauli-string exponentials:

$$
\begin{aligned}
&\exp\left(i\frac{\theta}{8}X_3Y_2X_1X_0\right)|0011\rangle \\
&= \left(\cos\left(\frac{\theta}{8}\right)I + i\sin\left(\frac{\theta}{8}\right)X_3Y_2X_1X_0\right)|0011\rangle \\
&= \left(\cos\left(\frac{\theta}{8}\right)I + i\sin\left(\frac{\theta}{8}\right)X_3X_2X_1Y_0Z_2Z_0\right)|0011\rangle \\
&= \left(\cos\left(\frac{\theta}{8}\right)I - i\sin\left(\frac{\theta}{8}\right)X_3X_2X_1Y_0\right)|0011\rangle \\
&= \exp\left(-i\frac{\theta}{8}X_3X_2X_1Y_0\right)|0011\rangle
\end{aligned} \tag{4.16}
$$

For the chosen HF ground state $|0011\rangle$, the ansatz simplifies to [61]:

$$
U = \exp\left(-i\frac{\theta_{1234}}{8}(X_3X_2X_1Y_0)\right) = \exp\left(-i\theta(X_3X_2X_1Y_0)\right) \tag{4.17}
$$

The quantum circuit implementation of the chemically inspired UCC ansatz is shown in Fig. 4.3.

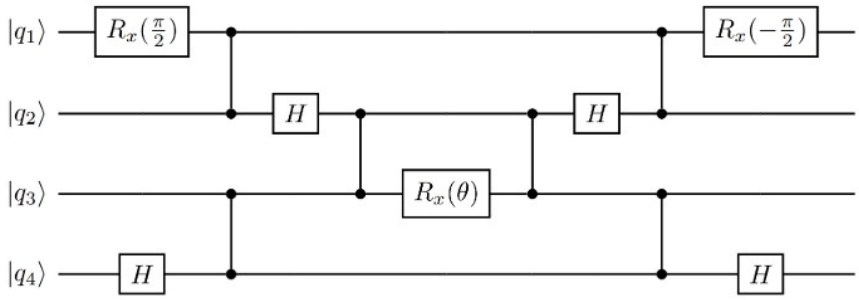



Figure 4.3: VQE circuit of the chemically-inspired UCC ansatz

By applying this ansatz, we perform VQE simulations for various values of $R$ and obtain the optimized ground-state energies.

Figure 4.4. $(a)$ presents the energy landscape as a function of the variational parameter $\theta$ for three different internuclear distances $R$. Each curve exhibits a well-defined minimum,

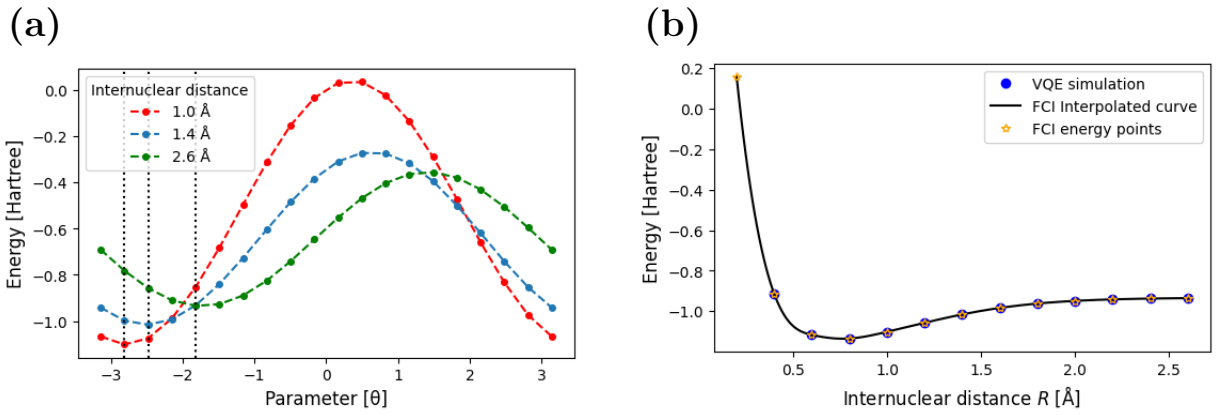



Figure 4.4: VQE simulation results: (a) Energy landscape of the variational optimization process for selected internuclear distances. (b) Ground-state energy curve from VQE simulations, compared with FCI reference values.

which corresponds to the optimized ground-state energy obtained via the VQE algorithm. The vertical dashed lines indicate the optimal values of $\theta$ for each case, demonstrating that the VQE procedure successfully identifies the energy minimum across different bond lengths. ($b$) shows the resulting energy curve obtained by extracting the minimum energy from similar energy landscapes across a range of internuclear distances. The VQE results (blue dots) closely follow the exact full configuration interaction (FCI) energies (black line), indicating that the ansatz and optimization procedure accurately capture the ground-state energy of $H_2$.

## 4.2 Impact of Noise on Ground-state Energy

### 4.2.1 Impact of Miscalibration on Variational Quantum Eigensolvers

Building upon our analysis of gate fidelity under voltage miscalibration, we now investigate its cumulative effect on a complete quantum algorithm—namely, the VQE. In the previous section, we demonstrated that different quantum gates exhibit varying sensitivity to two fundamental forms of voltage distortion: a multiplicative scaling factor $a$, sampled from a normal distribution with standard deviation $\sigma_a$, and an additive offset $b$, drawn from a normal distribution with standard deviation $\sigma_b$. These parameters model typical calibration

imperfections in control electronics. The distinct responses of single- and two-qubit gates to such distortions motivate a more detailed investigation of how miscalibration affects the performance of VQE circuits.

Here, we simulate the VQE procedure for estimating the ground-state energy of the hydrogen molecule under stochastic voltage miscalibration. For each VQE trial, we generate seven independent pairs of miscalibration parameters $(a_i, b_i)$, each sampled from $\mathcal{N}(1, \sigma_a^2)$ and $\mathcal{N}(0, \sigma_b^2)$, and apply them separately to all seven voltage channels in the system. These include four gate control voltages and three tunnel barrier voltages in our 4-quantum-dot simulator architecture. The distorted waveforms follow the miscalibrated pulse model introduced in Eq. (3.1), with each channel affected by its own unique miscalibration realization.

As shown in Fig. 4.5(a), increasing either $\sigma_a$ or $\sigma_b$ leads to a systematic overestimation of the ground-state energy $\langle E \rangle$. This upward bias aligns with perturbative intuition: calibration noise distorts gate operations, which collectively push the variational state away from the true ground state, resulting in higher energy estimates. Importantly, both types of miscalibration contribute monotonically to this effect, indicating that the VQE algorithm is broadly sensitive to deviations in both amplitude and offset of the control pulses. However, within a modest noise regime ($\sigma_a < 0.002$, $\sigma_b < 0.2$ mV), the algorithm maintains relatively accurate energy estimates, demonstrating **algorithmic robustness** against small calibration imperfections. This noise tolerance region defines a practical "reliability window" for multi-qubit quantum-dot systems.

Fig. 4.5(b) reports the corresponding standard deviation $\sigma_E$ of the energy estimates across repeated VQE runs with different noise realizations. The increase in $\sigma_E$ with noise strength reflects reduced algorithmic stability: As gate errors compound between operations, the final energy becomes more susceptible to noise. Notably, this variability is asymmetric, as seen in Fig. 4.5(d): the energy histogram exhibits a right-skewed shape with a longer tail toward higher energies. A gamma distribution provides an excellent fit, underscoring the non-Gaussian nature of error accumulation in quantum circuits.

Finally, Fig. 4.5(c) shows a smooth increase in energy deviation as $\sigma_a$ and $\sigma_b$ grow, reflecting the gradual degradation of variational accuracy across the explored noise range. At larger $\sigma_a$, the fidelity loss in entangling gates—particularly CZ—reduces the algorithm's ability to generate and maintain entanglement between qubits. In contrast, high $\sigma_b$ amplifies detuning errors that primarily perturb single-qubit rotations. Together, these effects produce a gate-dependent error landscape in which different control channels contribute unequally to overall performance loss.

In summary, voltage miscalibration impacts VQE through both systematic bias and

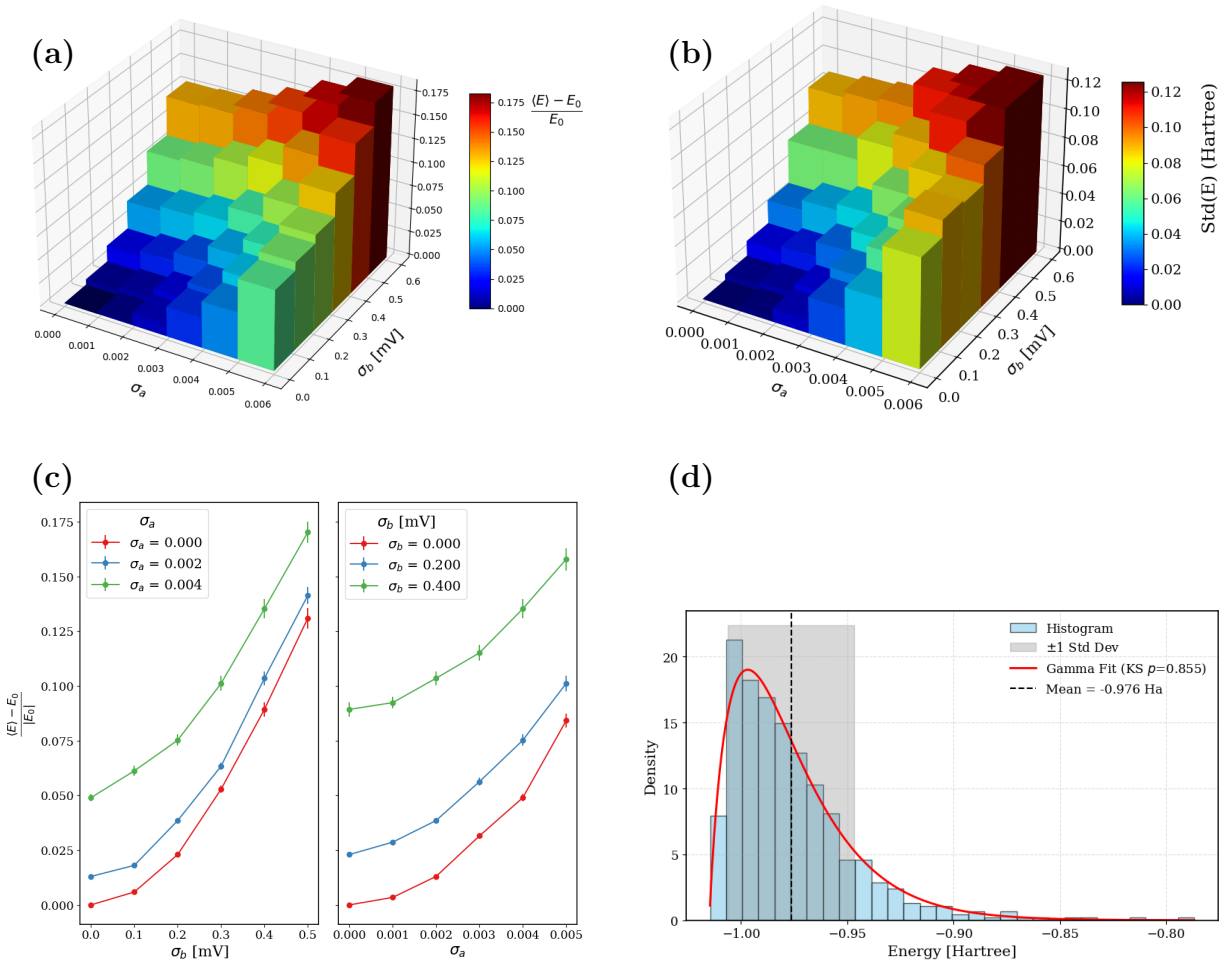



Figure 4.5: Effect of voltage miscalibration on VQE energy estimation from 600 independent VQE trials. (a) Average estimated energy $\langle E\rangle$ as a function of miscalibration strengths $\sigma_a$ and $\sigma_b$. (b) Standard deviation $\sigma_E$ of the energy estimates, showing increased fluctuations under noise. (c) Cross-sections of bar plots for $\langle E\rangle$ from (a) and (b), showing the dependence on $\sigma_b$ (with $\sigma_a$ fixed) and $\sigma_a$ (with $\sigma_b$ fixed). (d) Distribution of energy estimates for $\sigma_a = 0.002$, $\sigma_b = 0.0002$, fitted with a gamma distribution. The Kolmogorov–Smirnov (KS) test yields $p = 0.855$; since $p > 0.05$, there is no statistically significant deviation from the gamma fit, indicating a good agreement.

stochastic variability. The observed robustness for small $\sigma_a$ and $\sigma_b$ values underscores the feasibility of running variational algorithms on quantum-dot systems provided tight calibration control is achieved. Conversely, the findings motivate hardware designs with improved calibration stability and the development of adaptive error mitigation techniques for resilient variational quantum algorithms.

### 4.2.2 Impact of Random Telegraph Noise on Variational Quantum Eigensolvers

To complement the analysis of miscalibration errors, we now examine the effect of RTN on VQE performance. In our simulation, we model RTN as arising from multiple independent charge fluctuators distributed uniformly around the quantum dot array. The averaged noise signal applied to each gate voltage is given by an incoherent average of independent RTN sequences:

$$\mathrm{RTN}_{\mathrm{avg}}(t) = \frac{1}{\sqrt{N_{\mathrm{rtn}}}} \sum_{i=1}^{N_{\mathrm{rtn}}} \mathrm{rtn}_i(t),$$

where $N_{\mathrm{rtn}} = 50$ is the number of independent RTN sequences averaged to emulate a realistic ensemble of fluctuators, and each $\mathrm{rtn}_i(t)$ is characterized by a uniform switching rate $\tau^{-1}$ and equal noise amplitude $A$. Importantly, distinct $\mathrm{RTN}_{\mathrm{avg}}(t)$ signals are independently generated and applied to each electrode (both plunger and tunnel gates) in the simulated quantum processor.

The resulting relative error in the estimated ground-state energy of $H_2$ as a function of the RTN switching time $\tau$ and noise amplitude $A$ is shown in Fig. 4.2. The error metric is defined as

$$\epsilon = \log_{10}\left(\frac{\langle E\rangle - E_0}{|E_0|}\right),$$

where $\langle E\rangle$ is the VQE-estimated ground-state energy, and $E_0$ is the exact noise-free energy.

In the absence of noise, the VQE converges within a few minutes on our simulator. When RTN is included, however, the total runtime increases with the noise correlation time $\tau$, reflecting the slower convergence of the variational optimizer.

As shown in Fig. 4.6, the VQE energy error exhibits a distinct dependence on the RTN correlation time $\tau$. For small $\tau$ (high-frequency RTN, $\tau \lesssim 10^{-7}$ s), the error remains low and relatively insensitive to further decreases in $\tau$. This behavior is consistent with the

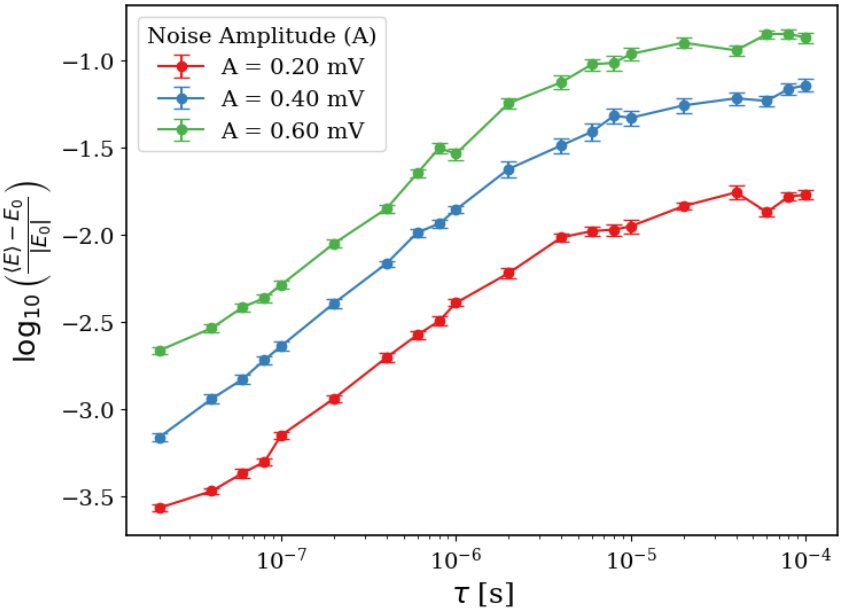



Figure 4.6: Relative error in the ground-state energy of the hydrogen molecule as a function of the RTN correlation time $\tau$, for three noise amplitudes $A$. The error bars represent standard deviations over 40 independent VQE runs.

dynamical averaging of high-frequency RTN: rapid switching leads to noise averaging out over the duration of single gate operations. Consequently, the variational algorithm retains a high degree of accuracy.

As $\tau$ increases into the intermediate regime ($10^{-7}$ s $\lesssim \tau \lesssim 10^{-5}$ s), the error grows polynomially. Here, the RTN switching rate becomes comparable to the gate operation time $t_{\text{gate}}$ and the total circuit duration $t_{\text{VQE}}$, allowing individual RTN trajectories to induce quasi-static shifts during a VQE run. These shifts accumulate over many quantum gate operations in the quantum circuit, leading to a systematic energy overestimation. Notably, the error saturates for large $\tau$ ($\tau \gtrsim 10^{-5}$ s), consistent with the quasi-static limit where each VQE trial experiences a fixed random voltage offset akin to miscalibration.

Furthermore, the logarithmic energy error grows approximately linearly with the noise amplitude $A$ across the entire $\tau$ range.

The transition between high-frequency and quasi-static regimes underscores the dual nature of RTN as both a stochastic and systematic error source. In the high-frequency regime, the RTN-induced errors are effectively depolarizing, introducing random fluctuations in gate fidelities. In contrast, in the quasi-static regime, RTN acts like a slowly varying miscalibration, shifting the variational landscape and degrading convergence.

**Implications.** This analysis highlights that VQE performance on quantum-dot architectures is particularly vulnerable to low-frequency RTN ($\tau \gtrsim t_{\text{VQE}}$) and large noise amplitudes ($A > 0.4$ mV). To maintain algorithmic robustness, it is crucial for hardware designs to minimize the presence of slow charge fluctuators, potentially through improved material engineering or dynamic compensation techniques. For high-frequency RTN ($\tau \ll t_{\text{gate}}$), the impact is minimal, suggesting that active error mitigation may be less critical in this regime.

Together with the miscalibration results, these findings establish quantitative benchmarks for voltage noise tolerances in quantum-dot platforms aiming to execute variational quantum algorithms reliably.

# Chapter 5

# Conclusions and future work

## 5.1 Conclusions

This thesis investigates the impact of control noise—particularly charge noise—on quantum-dot-based spin qubits, with a focus on its effect on quantum gates and algorithms implemented in silicon/silicon-dioxide ($Si/SiO_2$) architectures. Using a group-developed quantum-dot spin qubit simulator, we explored both systematic calibration errors and stochastic noise models, characterizing their influence on gate fidelities and algorithmic performance.

Chapter 2 detailed the methodology underpinning this study. We described how charge noise is modeled as a superposition of RTN sources to emulate $1/f$-type spectral characteristics. We then outlined how such noise sequences are added to the control voltages defining the quantum-dot potential landscape. The chapter also provided a concise introduction to QPT as a tool for characterizing noisy quantum operations.

In Chapter 3, we analyzed the effects of noise on individual quantum gates. We first examine the impact of voltage miscalibration, both multiplicative ($\sigma_a$) and additive ($\sigma_b$) errors—on the RX($\pi/2$), Hadamard, CZ, and $\sqrt{\text{SWAP}}$ gates. Due to the linear relationship between $\delta g$ and the gate voltage $V$, and the non-linear dependence of the exchange coupling $J$ on $V$, we observed marked differences in gate sensitivity. The RX($\pi/2$) and Hadamard gates, which rely solely on $\delta g$ and not on $J$, exhibited strong robustness against $\sigma_a$-type errors. In contrast, the CZ and $\sqrt{\text{SWAP}}$ gates, both of which depend on $J$, showed a higher sensitivity, particularly the latter. We supported these observations by deriving theoretical fidelity expressions for the RX and $\sqrt{\text{SWAP}}$ gates under miscalibration, which matched the simulation results with high accuracy.

Subsequently, we simulated the influence of RTN on all four gates. Across these gates, infidelity was found to increase approximately quadratically with noise amplitude, consistent with empirical fits of the form $1 - F \propto A^2$. For RX and Hadamard gates, infidelity monotonically increased with RTN correlation time $\tau$ a. In contrast, CZ and $\sqrt{\text{SWAP}}$ exhibited different behaviors: mid-frequency noise ($\tau \sim 10^{-5}$ s) dominated for CZ, while $\sqrt{\text{SWAP}}$ displayed the steepest growth in infidelity, underscoring its increased vulnerability to charge noise. The QPT analyzes then revealed the dominant error processes induced by RTN in each gate.

In Chapter 4, we extended the study to algorithm-level effects by simulating the variational quantum eigensolver (VQE) applied to compute the ground-state energy of a hydrogen molecule. Using our simulator, we successfully reproduced the VQE process and obtained energies consistent with theoretical expectations in the noise-free case. When miscalibration was introduced, we observed a systematic overestimation of $\langle E \rangle$ with increasing $\sigma_a$ and $\sigma_b$, reflecting the cumulative effect of gate imperfections. Importantly, the VQE algorithm demonstrated algorithm robustness within a practical noise regime, defining a 'reliability window' for multiqubit operations in quantum dots systems. For RTN, we identified a distinct dependence on $\tau$: high-frequency RTN ($\tau \lesssim 10^{-7}$ s) was effectively averaged out during gate operations, resulting in minimal impact on VQE accuracy.

Together, these findings provide a quantitative understanding of how charge noise propagates from single gates to quantum algorithms in silicon quantum-dot qubit systems.

## 5.2 Future Work

This work contributes to the growing body of knowledge on noise resilience in quantum-dot-based quantum computing platforms. Our analyses reveal that low-frequency charge noise, rather than high-frequency components, is the dominant source of error in silicon spin qubit systems—highlighting the need for noise suppression and calibration techniques that specifically target quasi-static fluctuations. Contrary to a common assumption, faster gate operations alone are insufficient to mitigate the impact of charge noise, as they only partially suppress high-frequency components that are not the primary error source.

By identifying a practical noise tolerance window, we provide a quantitative benchmark for experimentalists: within this regime, quantum algorithms such as VQE can achieve chemically accurate results despite realistic device imperfections. Moreover, our findings on the distinct error mechanisms—coherent versus incoherent—observed in QPT point toward noise-adapted control strategies and error mitigation protocols as promising directions for future research.

By bridging gate-level fidelity analyses with algorithm-level performance studies, this thesis offers actionable insights for error budgeting, control calibration, and the design of robust quantum algorithms. These results can inform the development of next-generation silicon quantum processors, accelerating progress toward fault-tolerant quantum computation.

Future research can build on this foundation in several directions:

- **Extension to multi-qubit algorithms:** While this work applied QPT primarily to single- and two-qubit gates, a natural next step is to extend such analyses to full multi-qubit algorithms. Applying QPT within variational algorithms like VQE or other quantum chemistry workflows would enable a detailed characterization of how gate-level noise propagates through complex circuits. This approach could reveal algorithm-specific error signatures, guide the development of noise-adapted ansätze, and inform error mitigation strategies in larger quantum-dot systems.
- **Integration of additional noise sources:** Charge noise dominates in Si-MOS systems, but other decoherence mechanisms—such as hyperfine interactions and spin-orbit coupling—should also be incorporated to capture a fuller picture of error sources.
- **Noise mitigation strategies:** Future studies could evaluate the efficacy of error suppression techniques such as dynamical decoupling, composite pulses, or noise-aware variational ansätze within the simulator.
- **Application to more complex algorithms:** Extending the analysis to other variational algorithms (e.g., QAOA) and quantum error correction codes could further reveal the interplay between noise and algorithmic resilience.

These directions will help advance the understanding and realization of robust quantum computation in silicon quantum-dot systems.

# References


[1] Jack D Hidary. *Quantum computing: an applied approach*, volume 1. Springer, 2021.

[2] Tiago M. Fernandez-Carames and Paula Fraga-Lamas. Towards post-quantum blockchain: A review on blockchain cryptography resistant to quantum computing attacks. *IEEE Access*, 8:21091–21116, 2020.

[3] Yudong Cao, Jonathan Romero, Jonathan P. Olson, Matthias Degroote, Peter D. Johnson, Mária Kieferová, Ian D. Kivlichan, Tim Menke, Borja Peropadre, Nicolas P. D. Sawaya, Sangmin Sim, Libor Veis, and Alán Aspuru-Guzik. Quantum chemistry in the age of quantum computing. *Chemical Reviews*, 119(19):10856–10915, 2019.

[4] E. R. MacQuarrie, C. Simon, S. Simmons, and E. Maine. The emerging commercial landscape of quantum computing. *Nature Reviews Physics*, 2(11):596–598, 2020.

[5] Mario Motta and Julia E. Rice. Emerging quantum computing algorithms for quantum chemistry. *Wiley Interdisciplinary Reviews: Computational Molecular Science*, 12(3):e1580, 2022.

[6] Han-Sen Zhong, Hui Wang, Yu-Heng Deng, Ming-Cheng Chen, Li-Chao Peng, Yan-Hong Luo, Jian Qin, Dian Wu, Xing Ding, Yi Hu, Peng Hu, Xiao-Yan Yang, Wei-Jun Zhang, Hui Li, Yu Li, Xue Jiang, Lin Gan, Guang Yang, Li You, Zhen Wang, Yi-Han Liu, Qi Ren, Yu He, Jie Zhang, Hao Li, Yu-Qing Zhang, Lei Zhang, Yong Xu, Nai-Le Li, Chao-Yang Lu, and Jian-Wei Pan. Quantum computational advantage using photons. *Science*, 370(6523):1460–1463, 2020.

[7] Frank Arute, Kunal Arya, Ryan Babbush, Dave Bacon, Joseph C. Bardin, Rami Barends, Rupak Biswas, Sergio Boixo, Fernando G. S. L. Brandao, David A. Buell, Brian Burkett, Yu Chen, Zijun Chen, Ben Chiaro, Rob Collins, William Courtney, Andrew Dunsworth, Edward Farhi, Brooks Foxen, Austin Fowler, Craig Gidney, Marissa Giustina, Rob Graff, Keith Guerin, Steve Habegger, Matthew P. Harrigan, Michael J.

Hartmann, Alan Ho, Markus Hoffmann, Trevor Huang, Travis S. Humble, Sergei V. Isakov, Evan Jeffrey, Zhang Jiang, Dorit Kafri, Kostyantyn Kechedzhi, Julian Kelly, Paul V. Klimov, Sergey Knysh, Alexander Korotkov, Felix Kostritsa, David Landhuis, Mike Lindmark, Erik Lucero, Dmitry Lyakh, Salvatore Mandrà, Jarrod R. McClean, Matt McEwen, Anthony Megrant, Xiaoying Mi, Kristel Michielsen, Masoud Mohseni, Josh Mutus, Ofer Naaman, Matthew Neeley, Charles Neill, Murphy Yuezhen Niu, Eric Ostby, Andrei Petukhov, John C. Platt, Chris Quintana, Eleanor G. Rieffel, Pedram Roushan, Nicholas C. Rubin, Daniel Sank, Kevin J. Satzinger, Vadim Smelyanskiy, Kevin J. Sung, Matthew D. Trevithick, Amit Vainsencher, Benjamin Villalonga, Theodore White, Z. Jamie Yao, Peter Yeh, Adam Zalcman, Hartmut Neven, and John M. Martinis. Quantum supremacy using a programmable superconducting processor. *Nature*, 574(7779):505–510, 2019.

[8] Yun-Hao Shi, Yu Liu, Yu-Ran Zhang, Zhongcheng Xiang, Kaixuan Huang, Tao Liu, Yong-Yi Wang, Jia-Chi Zhang, Cheng-Lin Deng, Gui-Han Liang, Zheng-Yang Mei, Hao Li, Tian-Ming Li, Wei-Guo Ma, Hao-Tian Liu, Chi-Tong Chen, Tong Liu, Ye Tian, Xiaohui Song, S. P. Zhao, Kai Xu, Dongning Zheng, Franco Nori, and Heng Fan. Quantum simulation of topological zero modes on a 41-qubit superconducting processor. *Phys. Rev. Lett.*, 131:080401, Aug 2023.

[9] John Clarke and Frank K. Wilhelm. Superconducting quantum bits. *Nature*, 453(7198):1031–1042, 2008.

[10] J. Ignacio Cirac and Peter Zoller. Quantum computations with cold trapped ions. *Physical Review Letters*, 74(20):4091–4094, 1995.

[11] E. Urban, T. A. Johnson, T. Henage, L. Isenhower, D. D. Yavuz, T. G. Walker, and M. Saffman. Observation of rydberg blockade between two atoms. *Nature Physics*, 5(2):110–114, 2009.

[12] B. E. Kane. A silicon-based nuclear spin quantum computer. *Nature*, 393(6681):133–137, 1998.

[13] D. DeMille. Quantum computation with trapped polar molecules. *Physical Review Letters*, 88(6):067901, 2002.

[14] Jacob Sevilla and Charles J. Riedel. Forecasting timelines of quantum computing, 2020.

[15] A. Ali Saki, M. Alam, and S. Ghosh. Study of decoherence in quantum computers: A circuit-design perspective, 2019.

[16] Qasim A. Memon, Mowafa Al Ahmad, and Michael Pecht. Quantum computing: Navigating the future of computation, challenges, and technological breakthroughs. *Quantum Reports*, 6(4):627–663, 2024.

[17] Guido Burkard, Thaddeus D. Ladd, Andrew Pan, John M. Nichol, and Jason R. Petta. Semiconductor spin qubits. *Reviews of Modern Physics*, 95(2):025003, 2023.

[18] A. M. Tyryshkin, J. J. L. Morton, S. C. Benjamin, A. Ardavan, G. A. D. Briggs, J. W. Ager, and S. A. Lyon. Coherence of spin qubits in silicon. *Journal of Physics: Condensed Matter*, 18(21):S783–S794, 2006.

[19] C. W. J. Beenakker. Theory of coulomb-blockade oscillations in the conductance of a quantum dot. *Physical Review B*, 44(4):1646–1656, 1991.

[20] Floris A. Zwanenburg, Andrew S. Dzurak, Andrea Morello, Michelle Y. Simmons, Lloyd C. L. Hollenberg, Gerhard Klimeck, Sven Rogge, Susan N. Coppersmith, and Mark A. Eriksson. Silicon quantum electronics. *Rev. Mod. Phys.*, 85:961–1019, Jul 2013.

[21] J. M. Taylor, J. R. Petta, A. C. Johnson, A. Yacoby, C. M. Marcus, and M. D. Lukin. Relaxation, dephasing, and quantum control of electron spins in double quantum dots. *Phys. Rev. B*, 76:035315, Jul 2007.

[22] Shannon P. Harvey. Quantum dots/spin qubits, February 2022.

[23] Guido Burkard, Daniel Loss, and David P. DiVincenzo. Coupled quantum dots as quantum gates. *Phys. Rev. B*, 59:2070–2078, 1999.

[24] F. H. Koppens, C. Buizert, K. J. Tielrooij, I. T. Vink, K. C. Nowack, T. Meunier, L. P. Kouwenhoven, and L. M. K. Vandersypen. Driven coherent oscillations of a single electron spin in a quantum dot. *Nature*, 442(7104):766–771, Aug 2006.

[25] M. Pioro-Ladrière, T. Obata, Y. Tokura, Y.-S. Shin, T. Kubo, K. Yoshida, T. Taniyama, and S. Tarucha. Electrically driven single-electron spin resonance in a slanting zeeman field. *Nature Physics*, 4:776–779, 2008.

[26] Guanjun Hu, Wenhui W. Huang, Rui Cai, Liang Wang, Chun-Hou Yang, Gang Cao, Xinyu Xue, Peng Huang, and Yutian He. Single-electron spin qubits in silicon for quantum computing. *Intelligent Computing*, 4:Article 0115, 2025.

[27] C. H. Yang, K. W. Chan, R. Harper, W. Huang, T. Evans, J. C. C. Hwang, B. Hensen, A. Laucht, T. Tanttu, F. E. Hudson, S. T. Flammia, K. M. Itoh, A. Morello, S. D. Bartlett, and A. S. Dzurak. Silicon qubit fidelities approaching incoherent noise limits via pulse engineering. *Nature Electronics*, 2(4):151–158, 2019.

[28] Menno Veldhorst, Jae C. C. Hwang, Chih-Hwan Yang, Adriaan W. Leenstra, Bram de Ronde, Juan P. Dehollain, Juha T. Muhonen, Fiona E. Hudson, Kohei M. Itoh, Andrea Morello, and Andrew S. Dzurak. An addressable quantum dot qubit with fault-tolerant control-fidelity. *Nature Nanotechnology*, 9(12):981–985, 2014.

[29] J. Y. Huang, R. Y. Su, W. H. Lim, M. Feng, B. van Straaten, B. Severin, W. Gilbert, N. Dumoulin Stuyck, T. Tanttu, S. Serrano, J. D. Cifuentes, I. Hansen, A. E. Seedhouse, E. Vahapoglu, R. C. C. Leon, N. V. Abrosimov, H.-J. Pohl, M. L. W. Thewalt, F. E. Hudson, and C. H. Yang. High-fidelity spin qubit operation and algorithmic initialization above 1 k. *Nature*, 627(8005):772–777, 2024.

[30] Tuomo Tanttu, W. H. Lim, J. Y. Huang, Niels Dumoulin Stuyck, William Gilbert, R. Y. Su, M. Feng, J. D. Cifuentes, A. E. Seedhouse, S. K. Seritan, C. I. Ostrove, K. M. Rudinger, R. C. C. Leon, W. Huang, C. C. Escott, K. M. Itoh, N. V. Abrosimov, H.-J. Pohl, M. L. W. Thewalt, and A. S. Dzurak. Assessment of the errors of high-fidelity two-qubit gates in silicon quantum dots. *Nature Physics*, 20(11):1804–1809, 2024.

[31] M. Rudolph, B. Sarabi, R. Murray, M. S. Carroll, and N. M. Zimmerman. Long-term drift of si-mos quantum dots with intentional donor implants. *Scientific Reports*, 9(1):7656, 2019.

[32] M. Kpa, N. Focke, Ł. Cywiński, and J. A. Krzywda. Simulation of 1 / f charge noise affecting a quantum dot in a si/sige structure. *Applied Physics Letters*, 123(3):034005, 07 2023.

[33] K. D. Petersson, J. R. Petta, H. Lu, and A. C. Gossard. Quantum coherence in a one-electron semiconductor charge qubit. *Phys. Rev. Lett.*, 105:246804, Dec 2010.

[34] Blake M. Freeman, Joshua S. Schoenfield, and HongWen Jiang. Comparison of low frequency charge noise in identically patterned si/sio2 and si/sige quantum dots. *Applied Physics Letters*, 108(25):253108, 06 2016.

[35] Jun Yoneda, Kenta Takeda, Takashi Otsuka, Takashi Nakajima, Mathieu R. Delbecq, Graham Allison, Takuya Honda, Tetsufumi Kodera, Shiro Oda, Yuki Hoshi, Noriko

Usami, Kohei M. Itoh, and Seigo Tarucha. A quantum-dot spin qubit with coherence limited by charge noise and fidelity higher than 99.9%. *Nature Nanotechnology*, 13(2):102–106, 2018.

[36] Stefan Birner, Tobias Zibold, Till Andlauer, Tillmann Kubis, Matthias Sabathil, Alex Trellakis, and Peter Vogl. nextnano: General purpose 3-d simulations. *IEEE Transactions on Electron Devices*, 54(9):2137–2142, 2007.

[37] B. Khromets, Z. D. Merino, and J. Baugh. Hamiltonian engineering with time-ordered evolution for unitary control of electron spins in semiconductor quantum dots. *arXiv preprint arXiv:2402.08146*, 2024.

[38] Ilias S. Kotsireas, Roderick Melnik, and Bryan West. *Advances in Mathematical and Computational Methods: Addressing Modern Challenges of Science, Technology, and Society*. AIP Press Imprint, New York, 2013. DOI: 10.1007/978-1-4614-6746-5.

[39] V. Celebonović. The hubbard model: Basic ideas and some results. *ACS Omega*, 8(30):26645–26649, 2023.

[40] E. Paladino, Y. M. Galperin, G. Falci, and B. L. Altshuler. $1/f$ noise: Implications for solid-state quantum information. *Reviews of Modern Physics*, 86(2):361–418, 2014.

[41] T. Itakura and Y. Tokura. Dephasing due to background charge fluctuations. arXiv preprint cond-mat/0303412, 2003.

[42] O. Gauthier, S. Haendler, P. Scheer, A. Vernhet, Q. Rafhay, and C. Theodorou. Enhanced statistical detection of random telegraph noise in frequency and time domain. *Solid-State Electronics*, 194:108320, 2022.

[43] Yoshihisa Yamamoto. *Fundamentals of Noise Processes*. Cambridge University Press, 2017.

[44] G. M. D'Ariano, M. G. A. Paris, and M. F. Sacchi. Quantum tomography. *arXiv preprint quant-ph/0302028*, 2003.

[45] D. Greenbaum. Introduction to quantum gate set tomography. *arXiv preprint arXiv:1509.02921*, 2015.

[46] C. Granade, C. Ferrie, and S. T. Flammia. Practical adaptive quantum tomography. *New Journal of Physics*, 19(11):113017, 2017.

[47] Z. Cai, R. Babbush, S. C. Benjamin, S. Endo, W. J. Huggins, Y. Li, J. R. McClean, and T. E. O'Brien. Quantum error mitigation. *Reviews of Modern Physics*, 95(4):045005, 2023.

[48] J. Roffe. Quantum error correction: an introductory guide. *Contemporary Physics*, 60(3):226–245, 2019.

[49] T. Luan, Z. Li, C. Zheng, X. Kuang, X. Yu, and Z. Zhang. Quantum tomography: From markovianity to non-markovianity. *Symmetry*, 16(2):180, 2024.

[50] Michael A. Nielsen and Isaac L. Chuang. *Quantum Computation and Quantum Information*. Cambridge University Press, Cambridge, 2000.

[51] Akshay Gaikwad, Arvind, and Kavita Dorai. True experimental reconstruction of quantum states and processes via convex optimization. *Quant. Inf. Proc.*, 20(1):19, 2021.

[52] A. N. Korotkov. Error matrices in quantum process tomography, 2013.

[53] Guido Burkard, Daniel Loss, David P. DiVincenzo, and John A. Smolin. Physical optimization of quantum error correction circuits. *Phys. Rev. B*, 60:11404–11416, Oct 1999.

[54] M. Veldhorst, C. H. Yang, J. C. C. Hwang, W. Huang, J. P. Dehollain, J. T. Muhonen, S. Simmons, A. Laucht, F. E. Hudson, K. M. Itoh, A. Morello, and A. S. Dzurak. A two-qubit logic gate in silicon. *Nature*, 526(7573):410–414, 2015.

[55] Y. Zhang, L. Cincio, C. F. A. Negre, I. Rungger, A. Andoni, and W. A. De Jong. Variational quantum eigensolver with reduced circuit complexity. *npj Quantum Information*, 8:96, 2022.

[56] D. A. Fedorov, B. Peng, N. Govind, and Y. Alexeev. VQE method: a short survey and recent developments. *Materials Theory*, 6:2, 2022.

[57] A. Wu, G. Li, Y. Wang, B. Feng, Y. Ding, and Y. Xie. Towards efficient ansatz architecture for variational quantum algorithms, 2021.

[58] E. J. Brandas and E. Brandas. *Preface*, volume 84, pages XI–XIII. Elsevier, 2021.

[59] P. Jordan and E. Wigner. Über das paulische Äquivalenzverbot. *Zeitschrift für Physik*, 47(9–10):631–651, 1928.

[60] David G. A. Smith, L. A. Burns, A. C. Simmonett, R. M. Parrish, M. C. Schieber, R. Galvelis, P. Kraus, H. Kruse, R. Di Remigio, A. Alenaizan, A. M. James, S. Lehtola, J. P. Misiewicz, M. Scheurer, R. A. Shaw, J. B. Schriber, Y. Xie, Z. L. Glick, D. A. Sirianni, and C. D. ... Sherrill. Psi4 1.4: Open-source software for high-throughput quantum chemistry. *The Journal of Chemical Physics*, 152(18):184108, 2020.

[61] Cornelius Hempel, Christine Maier, Jonathan Romero, Jarrod McClean, Thomas Monz, Heng Shen, Petar Jurcevic, Ben P. Lanyon, Peter Love, Ryan Babbush, Alán Aspuru-Guzik, Rainer Blatt, and Christian F. Roos. Quantum chemistry calculations on a trapped-ion quantum simulator. *Phys. Rev. X*, 8:031022, Jul 2018.

[62] S. M. Reimann and M. Manninen. Electronic structure of quantum dots. *Reviews of Modern Physics*, 74(4):1283–1342, 2002.

[63] W. G. van der Wiel, S. De Franceschi, J. M. Elzerman, T. Fujisawa, S. Tarucha, and L. P. Kouwenhoven. Electron transport through double quantum dots. *Rev. Mod. Phys.*, 75:1–22, Dec 2002.

[64] Michael Fogarty, Kok Wai Chan, Bas Hensen, Hans Huebl, Chih-Hwan Yang, Jae C. C. Hwang, Fiona E. Hudson, Kohei M. Itoh, Arne Laucht, Andrea Morello, and Andrew S. Dzurak. Integrated silicon qubit platform with single-spin addressability, exchange control and single-shot singlet-triplet readout. *Nature Communications*, 9(1):4370, 2018.

[65] A. M. J. Zwerver, T. Krähenmann, T. F. Watson, L. Lampert, H. C. George, R. Pillarisetty, S. A. Bojarski, P. Amin, S. V. Amitonov, J. M. Boter, R. Caudillo, D. Correas-Serrano, J. P. Dehollain, G. Droulers, E. M. Henry, R. Kotlyar, M. Lodari, F. Lüthi, D. J. Michalak, and J. S. ... Clarke. Qubits made by advanced semiconductor manufacturing. *Nature Electronics*, 5(3):184–190, 2022.

# APPENDICES

# Appendix A

# Coefficients for $R = 1.4\,\text{Å}$

Below are the coefficients calculated using the Python package Psi4 for an internuclear distance of $R = 1.4\,\text{Å}$:

| **Operator** | **Coefficient** |
|---|---|
| I | -0.473800316 |
| Z0 | 0.100535574 |
| Z1 | 0.100535574 |
| Z2 | -0.049032364 |
| Z3 | -0.049032364 |
| Z0 Z1 | 0.141204681 |
| Z0 Z2 | 0.086787499 |
| Z0 Z3 | 0.142543021 |
| Z1 Z2 | 0.142543021 |
| Z1 Z3 | 0.086787499 |
| Z2 Z3 | 0.148911897 |
| X0 X1 Y2 Y3 | -0.055755522 |
| X0 Y1 Y2 X3 | 0.055755522 |
| Y0 X1 X2 Y3 | 0.055755522 |
| Y0 Y1 X2 X3 | -0.055755522 |

Table A.1: Coefficients for $R = 1.4\,\text{Å}$ computed using Psi4.